

The JRA-55 Reanalysis: Representation of Atmospheric Circulation and Climate Variability

Yayoi HARADA, Hirotaka KAMAHORI, Chiaki KOBAYASHI, Hirokazu ENDO

Meteorological Research Institute, Japan Meteorological Agency, Tsukuba, Japan

**Shinya KOBAYASHI, Yukinari OTA, Hirokatsu ONODA, Kazutoshi ONOGI,
Kengo MIYAOKA, and Kiyotoshi TAKAHASHI**

Japan Meteorological Agency, Tokyo, Japan

(Manuscript received 15 July 2015, in final form 19 February 2016)

Abstract

This study investigates the quality of the Japanese 55-year Reanalysis (JRA-55), which is the second global reanalysis constructed by the Japan Meteorological Agency (JMA), by comparing it with other reanalyses and observational datasets. Improvements were found in the representation of atmospheric circulation on an isentropic surface and in the consistency of momentum budget based on the mass-weighted isentropic zonal mean method. The representation of climate variability in several regions was also examined. In the tropics, the frequencies of high spatial correlations with precipitation, which were estimated using the Tropical Rainfall Measuring Mission Multisatellite Precipitation Analysis, are clearly higher in JRA-55 than in JRA-25. The results indicate that JRA-55 generally improved the representations of phenomena on a wide range of space-time scales, such as equatorial waves, and transient eddies in the storm track regions, compared with JRA-25 during the satellite era. Moreover, JRA-55 improved the temporal consistency compared with the older reanalyses throughout the reanalysis period. In the stratosphere, we found larger discrepancies between reanalyses for the extra-tropical stratosphere during the Southern Hemisphere (SH) winter. Comparisons with radiosonde temperature revealed that JRA-55 has a smaller bias in temperature than the other reanalyses in the extra-tropical SH winter before 1979.

Some issues in JRA-55 were also identified. The amplitude of equatorial waves and Madden-Julian oscillation in JRA-55 are weaker than in the other reanalyses. JRA-55 shows unrealistic strong cooling in South America and Australia, although the spatial distribution of the long-term temperature trends in JRA-55 is the closest to an observational dataset of global historical surface temperature.

Keywords reanalysis; verification; climate variability; atmospheric circulation

1. Introduction

The Japan Meteorological Agency (JMA) has conducted the second global atmospheric reanalysis,

Corresponding author: Yayoi Harada, Meteorological Research Institute, 1-1 Nagamine, Tsukuba, Ibaraki 305-0052, Japan
E-mail: yharada@mri-jma.go.jp
©2016, Meteorological Society of Japan

i.e., the Japanese 55-year Reanalysis (JRA-55). This is the first comprehensive reanalysis to cover the last half-century since the European Centre for Medium-Range Weather Forecasts 45-year Reanalysis (ERA-40), and it is also the first to apply four-dimensional variational analysis (4D-Var) to this period. Kobayashi et al. (2015), in the first comprehensive report on JRA-55, outlined the general specifications and basic characteristics of this product. They

Table 1. Basic specifications of reanalyses used in this study.

Name	Organization	Reanalysis period	Resolution	Data assimilation method
JRA-55	JMA	1958 to present	TL319, L60 up to 0.1 hPa	4D-Var
JRA-25	JMA/CRIEPI	1979 to Jan. 2014	T106, L40 up to 0.4 hPa	3D-Var
ERA-40	ECMWF	Sep. 1957 to Aug. 2002	TL159, L60 up to 0.1 hPa	3D-Var
ERA-Interim	ECMWF	1979 to present	TL255, L60 up to 0.1 hPa	4D-Var
NCEP/NCAR	NCEP/NCAR	1948 to present	T62, L28 up to 3 hPa	3D-Var
NCEP-DOE2	NCEP/DOE	1979 to present	T62, L28 up to 3 hPa	3D-Var
CFSR	NCEP	1979 to present	T382, L64 up to 0.266 hPa	3D-Var (Coupled forecast system)
MERRA	NASA GMAO	1979 to present	(2/3)°×0.5°, L72 up to 0.01 hPa	3D-Var

described the JRA-55 system configuration including the data sources, quality control, data selection for observations, data assimilation system (DAS), and forecast model. In addition, they described two major improvements in quality over the Japanese 25-year Reanalysis (JRA-25; Onogi et al. 2007) product. One of the improvements is the reduction of dry bias in the Amazon basin, and another is the temporal consistency of temperature analysis.

The purpose of this study is to verify the representations of phenomena with various space–time scales in specific vertical and horizontal regions of the global atmosphere as well as those of atmospheric circulation and climate variability in JRA-55. We employ as many observational datasets as possible for the verification of various phenomena represented in JRA-55 and conduct comparisons with other reanalyses. The remainder of this manuscript is organized as follows. In Section 2, we describe the data and methods used in this investigation. Section 3 discusses improvements in the representation and consistency of the atmospheric flow. Sections 4, 5, and 6 focus on the representations of climate variability in the tropics, the extra-tropics, and the stratosphere, respectively. Section 7 presents the global distributions of long-term trends in surface air temperature. Finally, a summary and conclusions are provided in Section 8.

As described by Kobayashi et al. (2015), 27 independent Japanese researchers participated in quality evaluation prior to the release of the products. Their evaluations revealed the improvement of JRA-55 in various aspects. For example, they evaluated the signatures of naturally induced variability in the atmosphere (Mitchell et al. 2015), representation of the diurnal migrating tide in the stratosphere, extra-tropical cyclone activity, distribution of precipitation in the tropics, and diurnal cycle over East Asia (Chen et al. 2014). Some of these evaluation studies are included in this paper.

2. Data and methods

2.1 Reanalysis products for comparison

One of the purposes of this study is to clarify the advantages of JRA-55 over JRA-25. The detailed specifications of JRA-55 and JRA-25 were described by Kobayashi et al. (2015) and Onogi et al. (2007), respectively. In addition, we utilize products from other operational forecast centers and research institutes; the leading centers being European Center for Medium-range Weather Forecast (ECMWF), National Centers for Environmental Prediction (NCEP), National Aeronautics and Space Administration of Global Modeling and Assimilation Office (NASA GMAO), etc., as summarized in Table 1.

There are two major products of ECMWF; one is the ERA-40 reanalysis, the other is ERA-Interim. The ERA-40 reanalysis was generated with the three-dimensional variational (3D-Var) analysis version of the Integrated Forecasting System that was operational at ECMWF from June 2001 to January 2002 (Uppala et al. 2005). ERA-Interim is based on the 12-hourly 4D-Var analysis and includes many updates from ERA-40, such as variational bias correction to satellite radiance (Dee et al. 2011).

The major product from NASA GMAO is the Modern-Era Retrospective Analysis for Research and Applications (MERRA), which was generated with version 5.2.0 of the Goddard Earth Observing System (GEOS-5) atmospheric model and 3D-Var based DAS (Rienecker et al. 2011).

We also use the NCEP/National Center for Atmospheric Research (NCAR) reanalysis (NCEP/NCAR reanalysis; Kalnay et al. 1996; Kistler et al. 2001), which covers more than 66 years since 1948, a corrected version of the NCEP/NCAR reanalysis (NCEP-DOE reanalysis; Kanamitsu et al. 2002), and a new coupled global NCEP reanalysis called Climate Forecast System Reanalysis (CFSR; Saha et al. 2010).

2.2 Observational datasets for verification

This section describes the observational datasets used for verification.

Liebmann and Smith (1996) performed temporal and spatial interpolation of estimates of Outgoing Longwave Radiation (OLR) using National Oceanic and Atmospheric Administration (NOAA) polar orbiting satellites (Gruber and Krueger 1984), over a regular global grid, filled in the missing values at grid points not covered by the satellites. We utilize this interpolated daily OLR (NOAA OLR) at a horizontal resolution of $2.5^\circ \times 2.5^\circ$ in this study.

Huffman et al. (2007) estimated precipitation at fine scales ($0.5^\circ \times 0.5^\circ$ and 3 hourly) using the Tropical Rainfall Measuring Mission (TRMM) Multisatellite Precipitation Analysis (TMPA). In the TMPA framework, passive microwave data are collected from various low-earth-orbit satellites such as the Microwave Imager on TRMM, Special Sensor Microwave Imager (SSM/I) on Defense Meteorological Satellite Program satellites, Advanced Microwave Scanning Radiometer-Earth Observing System on the Aqua satellite, and Advanced Microwave Sounding Unit-B on the NOAA satellite series. Infrared data and monthly gauge data are also used. This estimated precipitation dataset is called TRMM3B42.

The best track for tropical cyclone verification was provided by Dr. M. Fiorino at the National Hurricane Center for the JRA-55 project (Fiorino 2002).

The Global Precipitation Climatology Centre (GPCC) has been conducting a global analysis of monthly land surface precipitation based on in situ rain-gauge data (Schneider et al. 2011). The full data reanalysis product (GPCC full ver. 6) is their most accurate product.

To verify the quality of sea level pressure (SLP) in reanalyses, we make use of an updated version of the Hadley Centre's monthly historical mean SLP (HadSLP2; Allan and Ansell 2006). HadSLP2 is constructed by blending surface pressure data from historical sources worldwide and from the International Comprehensive Ocean–Atmosphere Data Set (Worley et al. 2005).

The Earth Observing System Microwave Limb Sounder (MLS), onboard the National Aeronautics and Space Administration Aura satellite launched in July 2004 (Aura MLS), has been measuring temperatures, several atmospheric species, cloud ice, and geopotential heights to provide information about the earth's upper troposphere, stratosphere, and mesosphere (Waters et al. 2006). We calculate daily $2.5^\circ \times 2.5^\circ$ grid box-mean data using Aura MLS level 2

data and reanalyses. Note that box-mean values from reanalyses are used only when the corresponding box-mean value from Aura MLS is present.

The Hadley Centre and the Climatic Research Unit at the University of East Anglia (CRU) have collaborated and provided the global temperature series. Morice et al. (2012) updated the series to HadCRUT4, which is a combination of the new land air temperature CRUTEM4 (Jones et al. 2012) and the sea surface temperature (SST) analysis HadSST3 (Kennedy et al. 2011a, b). We make use of HadCRUT4 to verify the long-term trends in surface air temperature.

2.3 Methods

To examine datasets with different spatial resolutions, we bin the data into common grid cells with a horizontal resolution of $2.5^\circ \times 2.5^\circ$ or $5^\circ \times 5^\circ$ to calculate the differences between the datasets. To ensure comparability, the end of the reference period was chosen to be 2001 when JRA-55 was compared with ERA-40.

To extract the various atmospheric waves or disturbances, we apply a Lanczos filter (Duchon 1979) to the daily OLR and the daily zonal and meridional wind components of the reanalysis products. We investigate the activity of equatorial waves (Section 4.2) and synoptic variability in storm track regions at mid-latitudes (Section 5.2).

3. Representation and consistency of atmospheric flow

3.1 Improvements in the representation of atmospheric flow

In the DAS of JRA-55, new radiation and advection schemes are included in the forecast model and 4D-Var with variational bias correction to satellite radiances is implemented (Kobayashi et al. 2015). Hence, it is expected that JRA-55 improves the representation of atmospheric flow and the temporal consistency. We attempt to verify and visualize the improvements in the atmospheric flow in the upper troposphere. Previous studies have shown that Ertel potential vorticity (PV) is conserved for adiabatic, frictionless motion and that it acts as a tracer of the atmospheric flow on an isentropic surface (Hoskins et al. 1985). Therefore, it is reasonable to verify the representations of atmospheric flow and circulation in reanalyses using PV on the isentropic surface. Figure 1 shows an example of the spatial PV distribution on a 360 K isentropic surface. Focusing on a high PV anomaly to the southwest of Japan, which

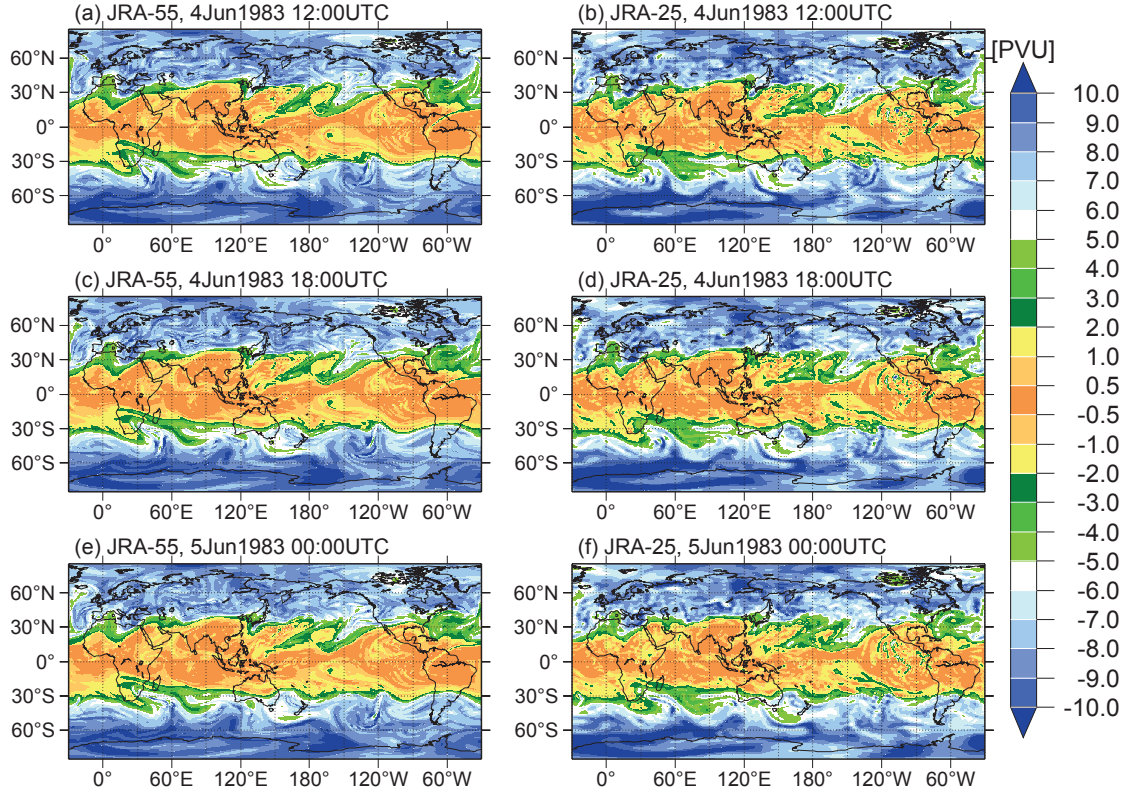


Fig. 1. Field of isentropic potential vorticity map at 360 K. Unit: PVU ($1 \text{ PVU} = 10^{-6} \text{ m}^2 \text{ s}^{-1} \text{ K kg}^{-1}$).

means a higher value than that of its environmental field, not deviation from the climatological mean, it is apparent that the temporal consistency of JRA-55 (Figs. 1a, c, e) is far superior to that of JRA-25 (Figs. 1b, d, f). Moreover, the scattered distribution of PV is observable for JRA-25, while it is not seen in JRA-55. In JRA-25, an Eulerian scheme and 3D-Var were utilized. Eulerian schemes tend to have significant dispersion errors in fine-scaled humidity fields (Ritchie 1985). In addition, 3D-Var does not take account of observational time accurately. These would be related to the differences between the abovementioned analyses.

3.2 Consistency of zonal mean fields

In this subsection, we focus on the consistency of the atmospheric flow in the zonal mean fields. To verify the representation and consistency of atmospheric flow, we use the mass-weighted isentropic zonal mean (MIM) method developed by Iwasaki (1989) (see also Iwasaki 1990, 1992, 1998; Tanaka et al. 2004). The zonal mean primitive equation is

used, and the vertical coordinate is defined by the isentropic zonal mean pressure. All variables representing the zonal mean field are zonally averaged with normalized weights proportional to the air mass between two isentropic surfaces:

$$\overline{A(\phi, \theta, t)}^* \equiv \frac{1}{2\pi} \int A(\lambda, \phi, \theta, t) \left(\frac{\partial p}{\partial \theta} / \overline{\frac{\partial p}{\partial \theta}} \right) d\lambda, \quad (1)$$

where A represents a physical quantity, and λ, ϕ, θ, t , and p are longitude, latitude, potential temperature, time, and pressure, respectively. The overbars and asterisks denote isentropic zonal mean and local mass weight normalized by its zonal mean, respectively.

The zonal-mean zonal momentum equation and Eliassen–Palm flux (EP flux) are represented as follows:

$$\begin{aligned} \frac{\partial \overline{u}^*}{\partial t} = & - \frac{\overline{v}^*}{a \cos \phi} \frac{\partial \overline{u}^*}{\partial \phi} \cos \phi - \overline{w}_\dagger^* \frac{\partial \overline{u}^*}{\partial z_\dagger} + f \overline{v}^* \\ & + \frac{\nabla \bullet F}{a \rho_0 \cos \phi} + \overline{X}^*, \end{aligned} \quad (2)$$

$$\mathbf{F} = \rho_0 a \cos \phi \left(-\overline{(u'v')^*}, -\overline{(u'w')^*} \right. \\ \left. + \frac{1}{\rho_0 g a \cos \phi} \overline{p \left(\frac{\partial \Phi}{\partial \lambda} \right)_{p\dagger}} \right), \quad (3)$$

where a , f , u , v , w , and X are the earth's radius, Coriolis parameter, zonal velocity, meridional velocity, vertical velocity, and frictional forcing, respectively, and \mathbf{F} , ρ_0 , g , and Φ are EP flux, reference density, gravitational acceleration, and geopotential, respectively. Daggers denote isentropic zonal means, and the log-pressure coordinate for isentropic zonal mean pressure is given by $Z_\dagger \equiv -H \log(p_\dagger/p_0)$, where H is scale height.

In the MIM framework, adiabatic wave motion, which produces a Stokes drift, is separated from diabatic effects, and the MIM method enables analysis of a single hemispheric cell, such as the Brewer-Dobson circulation (BDC) in the stratosphere and the tropospheric direct circulation. We apply the MIM method to JRA-55 and JRA-25 model grid data and calculate the regional average value of each term in Eq. (2). Using this method, the zonal-mean zonal wind acceleration was found to balance the sum of the forcing terms on the right side of the zonal mean equation (Eq. 2). However, in actual data assimilation, the analysis increment, which is defined as analysis minus first guess (6-hourly forecast in this case), disturbs these terms, resulting in an imbalance in the momentum budget. Kobayashi et al. (2015) showed that global mean of root-mean-square (RMS) departures (or differences) from radiosonde temperatures decreased in JRA-55. In this study, we assess whether the improved fit to observations contributes to balancing the zonal momentum budget.

Figure 2 shows latitude-pressure cross-sections of zonal-mean zonal wind and its RMS analysis increment averaged over Northern Hemisphere (NH) winters (December–February) from 1979/1980 to 2011/2012. While the features of the zonal-mean zonal wind in JRA-55 (Fig. 2a) and JRA-25 (Fig. 2b) are generally consistent, the RMS analysis increments of the zonal-mean zonal wind in the extratropics for both the upper troposphere and the upper stratosphere are greatly reduced in JRA-55 (Fig. 2c) compared with the corresponding values in JRA-25 (Fig. 2d). Furthermore, focusing on the mass stream function (Fig. 3), the analysis increments in the troposphere in JRA-25 (Fig. 3d) are greatly reduced in JRA-55 (Fig. 3c). The reduction is related to the fact that the numerical weather prediction model in the DAS of JRA-55 is better than that in JRA-25. In

the lower stratosphere, the BDC of JRA-55 (Fig. 3a) is slightly weaker than that of JRA-25 (Fig. 3b). For example, the line of $0.61 \times 10^{10} \text{ kg s}^{-1}$ is observable above the 50 hPa level in JRA-25, while it is seen below the 50 hPa level in JRA-55. In reanalysis datasets, the BDC characteristics are dependent on the data assimilation scheme and the forecast models used to generate the first-guess field (Iwasaki et al. 2009). The annual- and seasonal-mean upwelling of JRA-55 is weaker than that of JRA-25 and has very similar values to ERA-Interim at selected vertical levels (Fig. 4). Because the thermodynamic balance of JRA-55 is much better than that of JRA-25 (Kobayashi and Iwasaki 2016), the BDC strength diagnosed using JRA-55 is higher than that from JRA-25.

Figure 5 depicts the zonal momentum budgets averaged over $45\text{--}60^\circ\text{N}$ during the major sudden stratospheric warming (SSW) event that occurred in mid-January 2009 (Harada et al. 2010). SSW events usually occur due to the upward propagation of planetary-scale wave packets from the troposphere, and the convergence of these wave packets causes deceleration of zonal-mean zonal wind in the stratosphere. The agreement between the zonal mean wind acceleration (the black lines in Fig. 5) and the sum of forcing terms (the red lines in Fig. 5) indicates the consistency of the zonal momentum budget. In JRA-25 at the 5 hPa level, the sum of forcing terms does not follow the zonal mean wind acceleration around the peak of the zonal wind deceleration (Fig. 5d). In contrast, in JRA-55, the sum of forcing terms closely follows the zonal mean wind acceleration even at the peak of the zonal wind deceleration (Fig. 5c). Moreover, at other pressure levels, JRA-55 shows good agreement between the zonal wind acceleration and the sum of forcing terms throughout the entire period. This feature is common in other major SSW events (not shown).

As mentioned above, both the reduction of biases in the general circulation fields and a more consistent zonal momentum budget are clearly observable in JRA-55. These results indicate improvement in the representation of the global atmospheric circulation in JRA-55.

4. Climate variability in the tropics

4.1 Validation of precipitation in the tropics

Kobayashi et al. (2015) presented climatologies of global precipitation distributions for several reanalyses and an observational dataset based on a monthly mean timescale promoted by The Global Precipitation Climatology Project (GPCP, Adler et al. 2003).

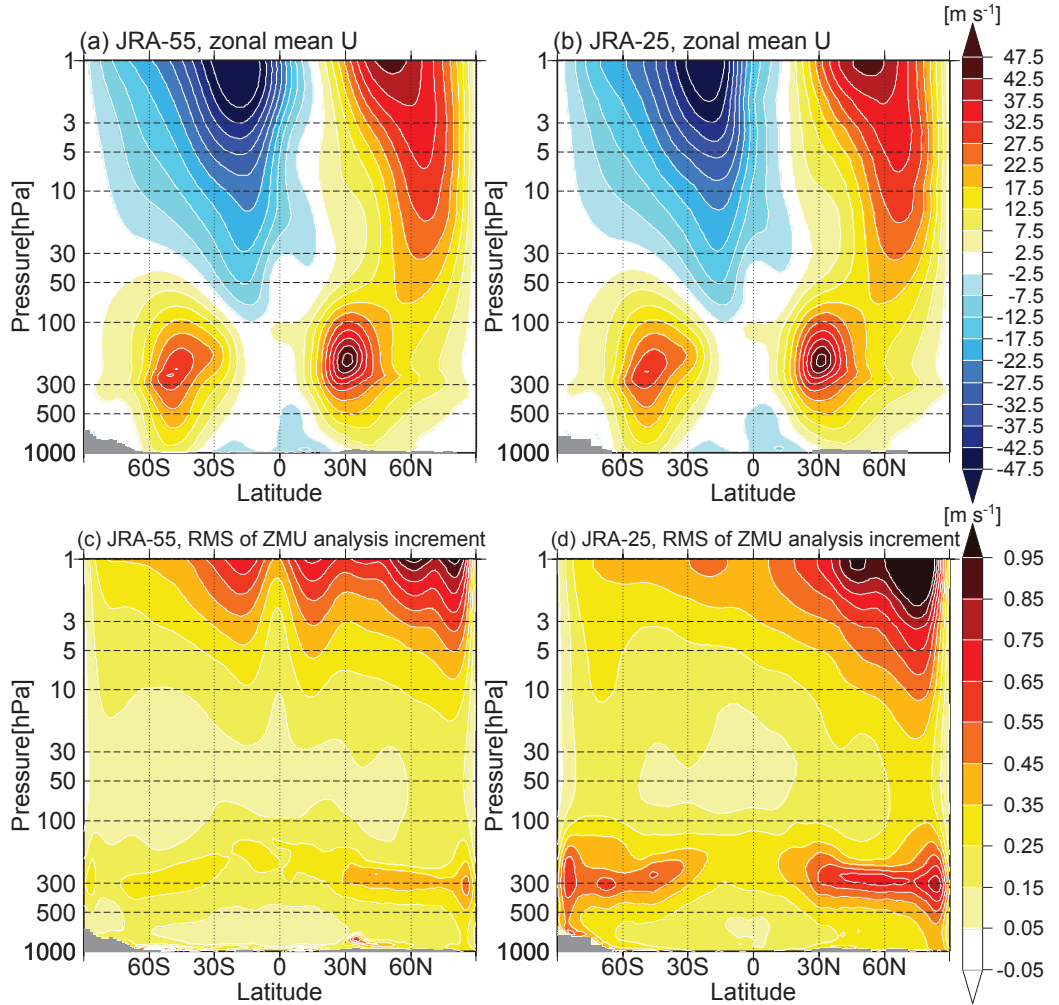


Fig. 2. Latitude–pressure cross-sections of (a, b) zonal-mean zonal wind and (c, d) its RMS analysis increment over the NH winters (December–February) from 1979/1980 to 2011/2012 for (a, c) JRA-55 and (b, d) JRA-25.

In this section, we focus on the representation of tropical precipitation for shorter timescales against TRMM3B42 (Huffman et al. 2007; see also Section 2.2). The forecast model used in JRA-55 implements higher resolutions in both the horizontal and vertical directions compared with that in JRA-25. Therefore, it is expected that JRA-55 products have an improved representation of the distribution of precipitation for smaller and shorter space–time scales than typical scales in monthly data.

Figure 6 shows the frequency of the spatial correlation of the daily mean precipitation over the tropics with TRMM3B42 from 1998 to 2009. The frequencies of high spatial correlations are clearly

higher in JRA-55 (red diamonds) than in the NCEP/NCAR reanalysis (right blue circles), JRA-25 (pink diamonds), CFSR (blue crosses), and ERA-Interim (green triangles) and are close to those in MERRA (purple crosses). This result indicates that JRA-55 has higher quality in the representation of daily precipitation in the tropics. However, as mentioned by Kobayashi et al. (2015), JRA-55 overestimates the precipitation in the tropics compared with the observational precipitation dataset GPCP. Compared with TRMM3B42, JRA-55 tends to overestimate the area-mean precipitation rates for weak precipitation under suppressed convection (Fig. 7a). The other reanalyses used for comparison are similar to JRA-55 in this

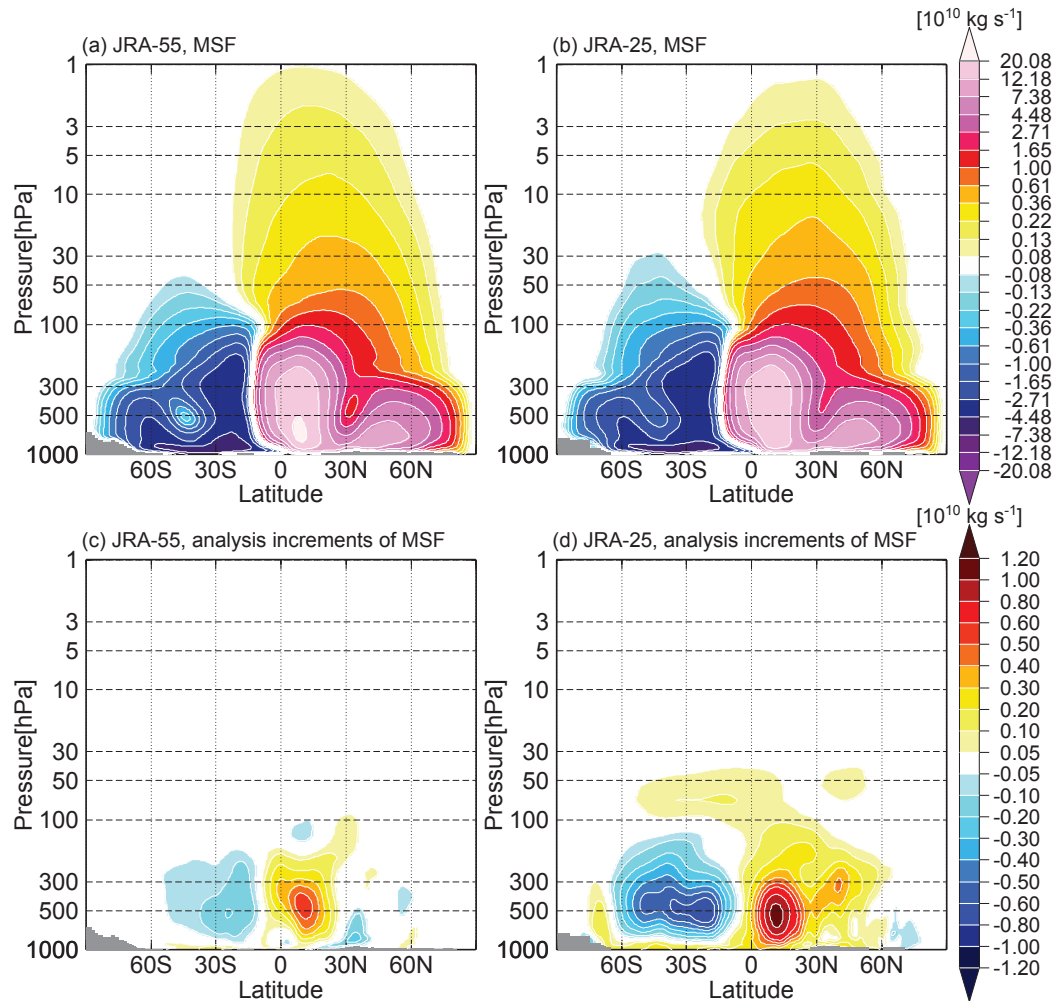


Fig. 3. As in Fig. 2, but for (a, b) mass stream function and (c, d) its analysis increments.

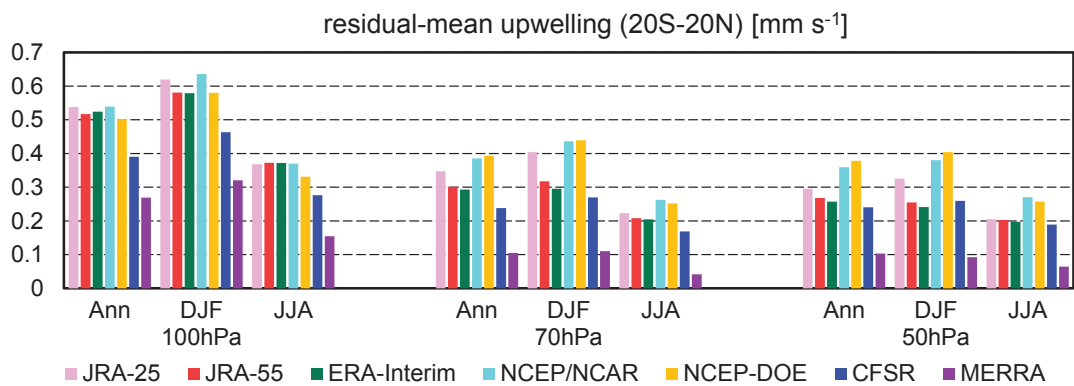


Fig. 4. Annual and seasonal mean residual-mean upwelling within 20° of the equator, averaged from 1979 to 2012.

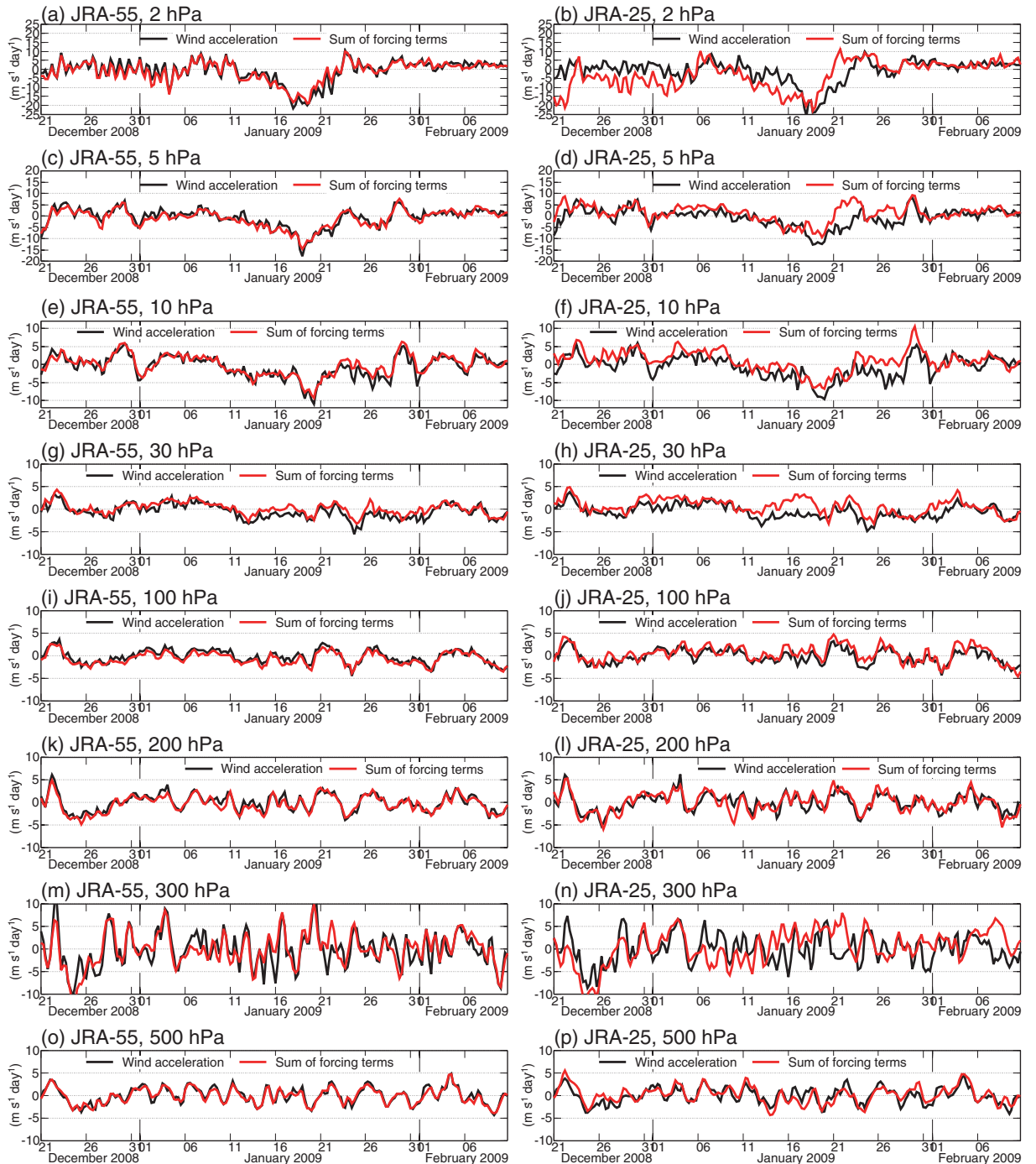


Fig. 5. Zonal momentum budgets averaged over 45–60°N during the major sudden stratospheric warming that occurred in mid-January 2009. The black lines show zonal mean wind acceleration and the red lines show the sums of advection, Coriolis forcing, EP flux divergence, and frictional forcing terms.

regard, and all of the reanalyses overestimates precipitation when the TRMM3B42 precipitation is less than

4 mm day^{-1} .

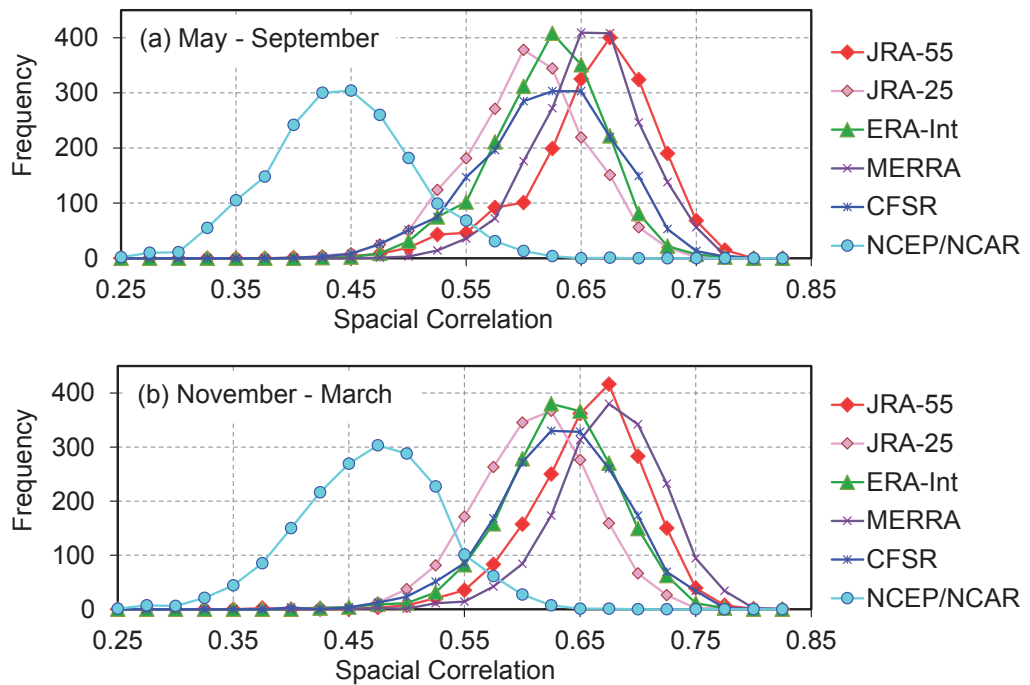


Fig. 6. Frequency of spatial correlation of daily mean precipitation with TRMM3B42 over the tropics (22°S – 22°N) from 1998 to 2009.

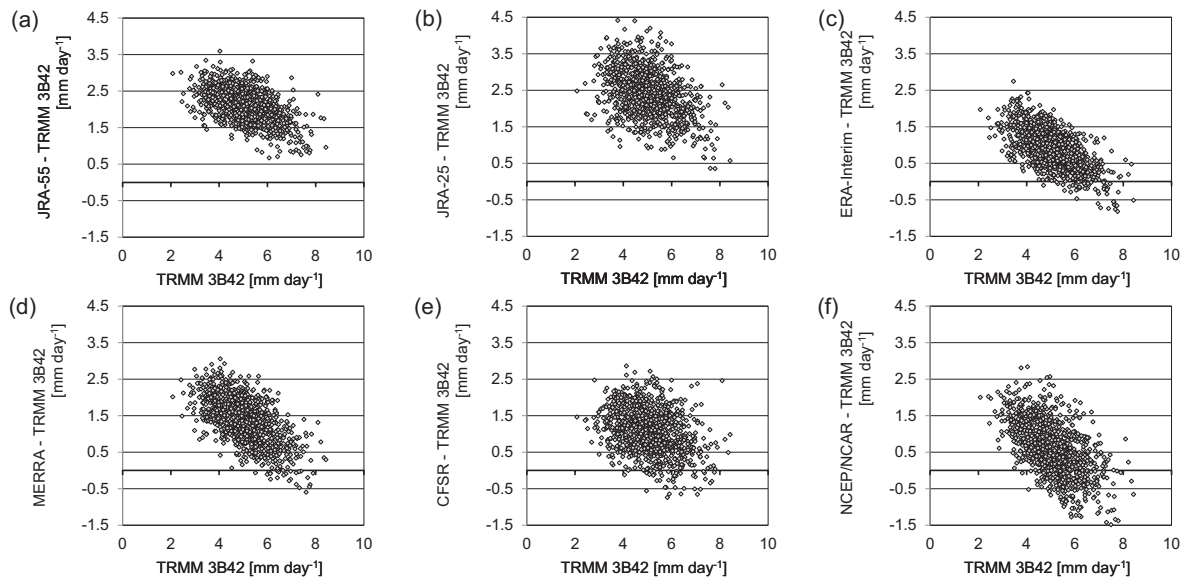


Fig. 7. Scatter diagrams of 22°S – 22°N , 90 – 160°E averaged daily precipitation between TRMM 3B42 and the difference between the reanalysis and TRMM3B42 during the NH warm season (May–September) from 2003 to 2009.

4.2 Convectively coupled equatorial waves and Madden-Julian oscillation

The tropical or equatorial regions contain waves with various space-time scales, such as convectively coupled Kelvin waves, equatorial Rossby (ER) waves, and mixed Rossby-gravity (MRG) waves. In addition, the Madden-Julian oscillation (MJO) is the dominant mode on an intra-seasonal timescale. Numerous studies have been conducted using reanalysis data, and recently Kim et al. (2014) evaluated the tropical variability of precipitation from five global reanalysis by comparison with an observational dataset. Fujiwara et al. (2012) also investigated wave activity in the tropical tropopause layer in seven reanalyses. As discussed in these studies, the representations of the equatorial waves and MJO are one of the most important aspects of reanalysis quality. To verify the representation of convectively coupled equatorial waves, we conducted a wavenumber-frequency power spectrum analysis following Wheeler and Kiladis (1999). They performed a wavenumber-frequency spectrum analysis for longitudes in the domain 15°S – 15°N using the daily NOAA OLR, decomposed the data into symmetric and antisymmetric components, and isolated several statistically significant spectral peaks. We apply this method to the OLR estimated from several reanalyses and compare the results of reanalyses with those of NOAA OLR. Figure 8 shows the zonal wavenumber-frequency power spectrum ratio of OLR to its background (defined as an average of smoothed symmetric and antisymmetric components) within 15°S – 15°N for the period from January 1981 to December 2001. For the symmetric component (upper panels in Fig. 8) comparison with NOAA OLR (Fig. 8h) shows that the reanalyses generally depict the MJO signal, but some of them tend to be weaker than that of NOAA OLR, while the MJO signals in JRA-55 (Fig. 8a) and ERA-Interim (Fig. 8d) are stronger than in the other reanalyses and are closer to those in the NOAA OLR case (Fig. 8h). Moreover, the Kelvin wave signal in JRA-55 is stronger than the others and is rather close to that in the NOAA OLR case. On the other hand, the ER wave signal in JRA-55 is weaker than it is in ERA-Interim (Fig. 8d), MERRA (Fig. 8e), and CFSR (Fig. 8f), which are closer to the NOAA OLR case. For the antisymmetric component (lower panels in Fig. 8), although the MRG wave signals in the reanalyses are much weaker than they are in NOAA OLR (Fig. 8p), it is noteworthy that the MRG wave signal in JRA-55 (Fig. 8i) is stronger than those in the other reanalyses. Moreover, before 1978, the signals of the

equatorial waves and the MJO in JRA-55 (Fig. 9a) are much stronger than those in ERA-40 and the NCEP/NCAR reanalysis (Figs. 9b, c). This result indicates that the quality of JRA-55 is consistent throughout its reanalysis period.

One noteworthy issue is related to the variability in equatorial waves and the MJO. JRA-55 underestimates the background power spectrum of OLR (not shown). Therefore, the amplitudes of equatorial waves and the MJO in JRA-55 are weaker than they are in the other reanalyses during the whole reanalysis period. Figure 10 shows the longitudinal distribution of 20–100-day band-pass-filtered OLR variability averaged over 3°S – 3°N for the period from 1980 to 2001. In particular, the amplitude of the MJO is very weak in the Indian Ocean and the western Pacific. This feature is commonly observed for equatorial waves (not shown). Yokoi (2015) compared three reanalyses (JRA-55, JRA-25, and ERA-Interim) with column water vapor (CWV) and precipitation retrieved from SSM/I, focusing on intra-seasonal variability in the tropics, and noted that while the forecast model used for JRA-55 is able to simulate eastward propagation of such CWV anomalies, it tends to weaken their amplitudes due to the excessively weak cloud-radiative feedback in the forecast model.

4.3 Representation of position and intensity of tropical cyclones

To represent tropical cyclones (TCs) reasonably well in data-sparse areas such as the tropical oceans, JRA-55 assimilates tropical cyclone wind retrievals (TCRs, Fiorino 2002) which are derived from best track data to mimic radiosonde observations, as used in JRA-25 (Fiorino 2002). Kobayashi et al. (2015) found that JRA-55 represents around 95 % of the 6 hour global TC frequencies observed for the period from the 1950s to the 1980s and 85–90 % in the 2000s. On the other hand, ERA-Interim, which does not assimilate artificial TC information such as TCRs, detects 60 % in the 1980s and 75–80 % in the 2000s. The differences in the TC detection rates of JRA-55 and ERA-Interim demonstrate the usefulness of TCRs in TC representation. Murakami (2014) evaluated and compared the reproducibility of TCs in JRA-55, JRA-25, ERA-40, ERA-Interim, CFSR, and MERRA and found that JRA-55 was the best of the six reanalyses in terms of the skill of the spatial and temporal distribution of TC frequency. Here, we evaluate TC representation in JRA-55 in terms of position and intensity by comparison with the best track as well as with JRA-25 and ERA-Interim.

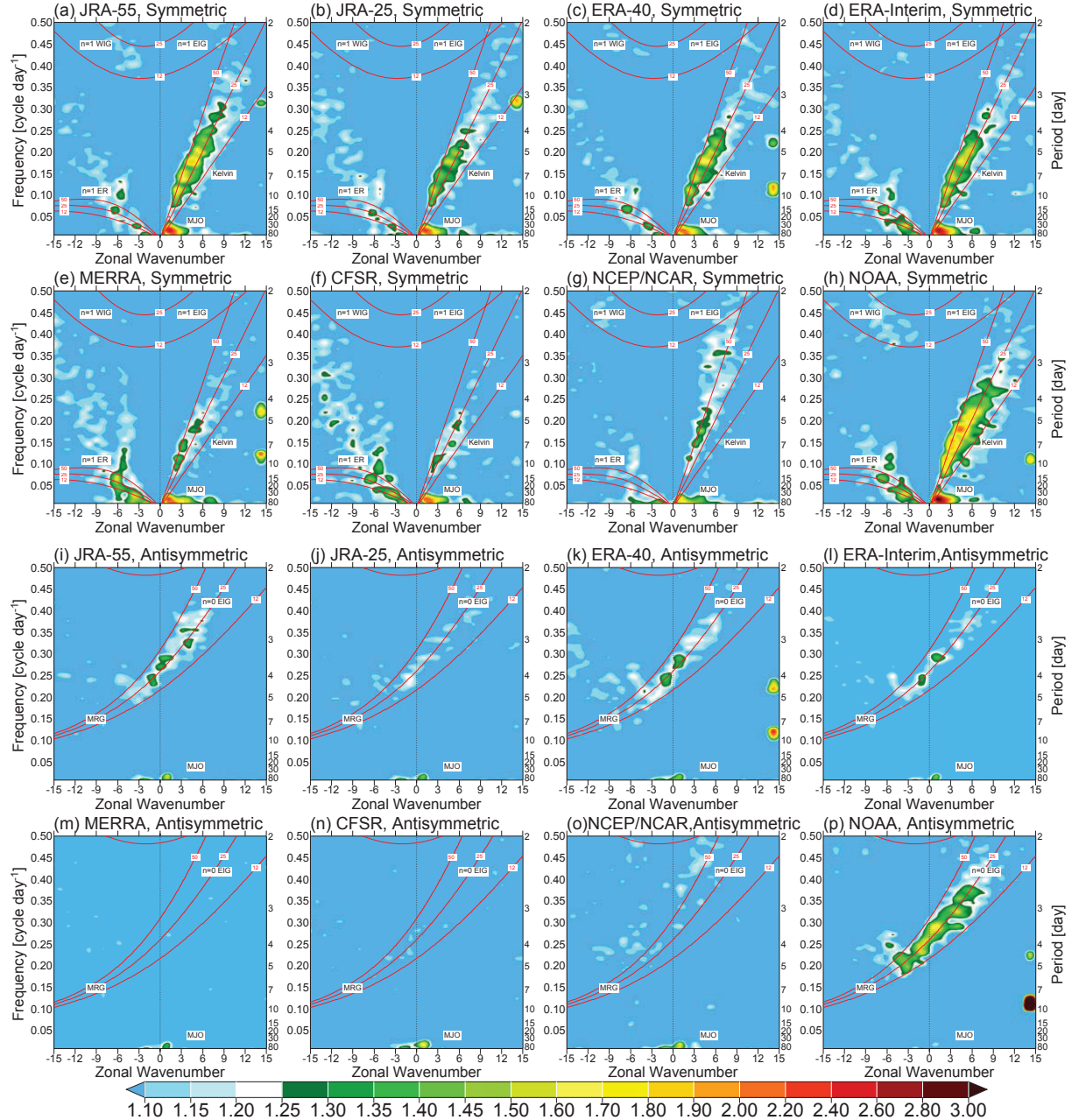


Fig. 8. Zonal wave number–frequency power spectrum ratio (Wheeler and Kiladis 1999) of OLR divided by its background (defined as average of smoothed symmetric and antisymmetric components) within 15°S – 15°N from January 1981 to December 2001 for (a, i) JRA-55, (b, j) JRA-25, (c, k) ERA-40, (d, l) ERA-Interim, (e, m) MERRA, (f, n) CFSR, (g, o) NCEP/NCAR reanalysis, and (h, p) NOAA OLR. Upper (lower) panels show symmetric (antisymmetric) components.

Figures 11 and 12 show the geographical distribution and zonal mean climatology, respectively, of the root mean square errors (RMSEs) of the differ-

ences between the TC center positions reproduced in JRA-55, JRA-25, and ERA-Interim against the best track. Here, climatology is defined as the average

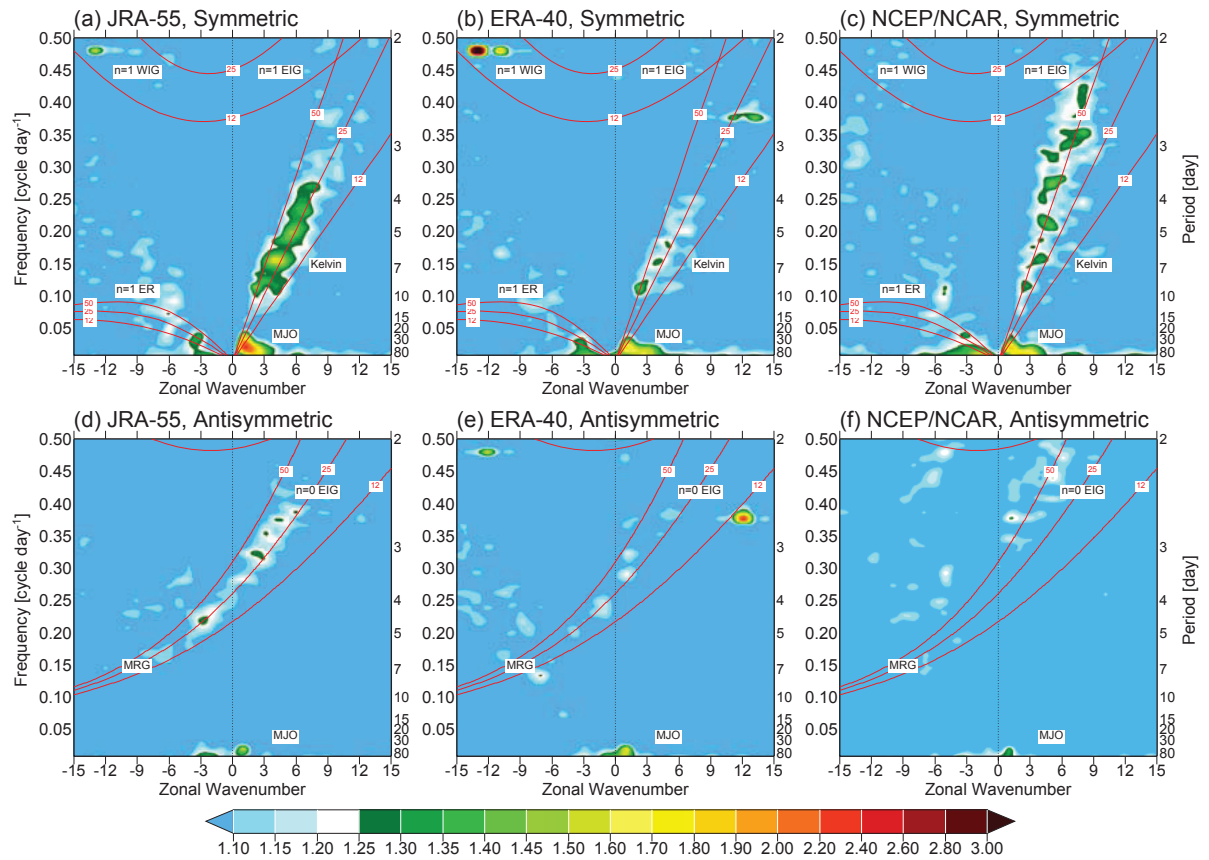


Fig. 9. As in Fig. 8, but from January 1958 to December 1978 for (a, d) JRA-55, (b, e) ERA-40, and (c, f) the NCEP/NCAR reanalysis.

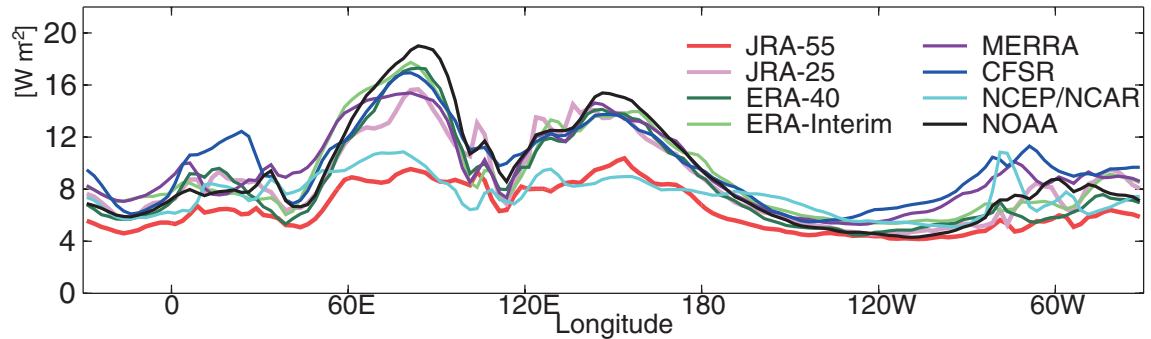


Fig. 10. Longitudinal distribution of 20–100-day band-pass-filtered OLR variability averaged over 3°S–3°N from 1980 to 2001.

for 1981–2010, and the zonal mean includes only non-missing grid points. Schenkel and Hart (2012)

evaluated the mean difference between the TC positions in the reanalyses and the best track. Because

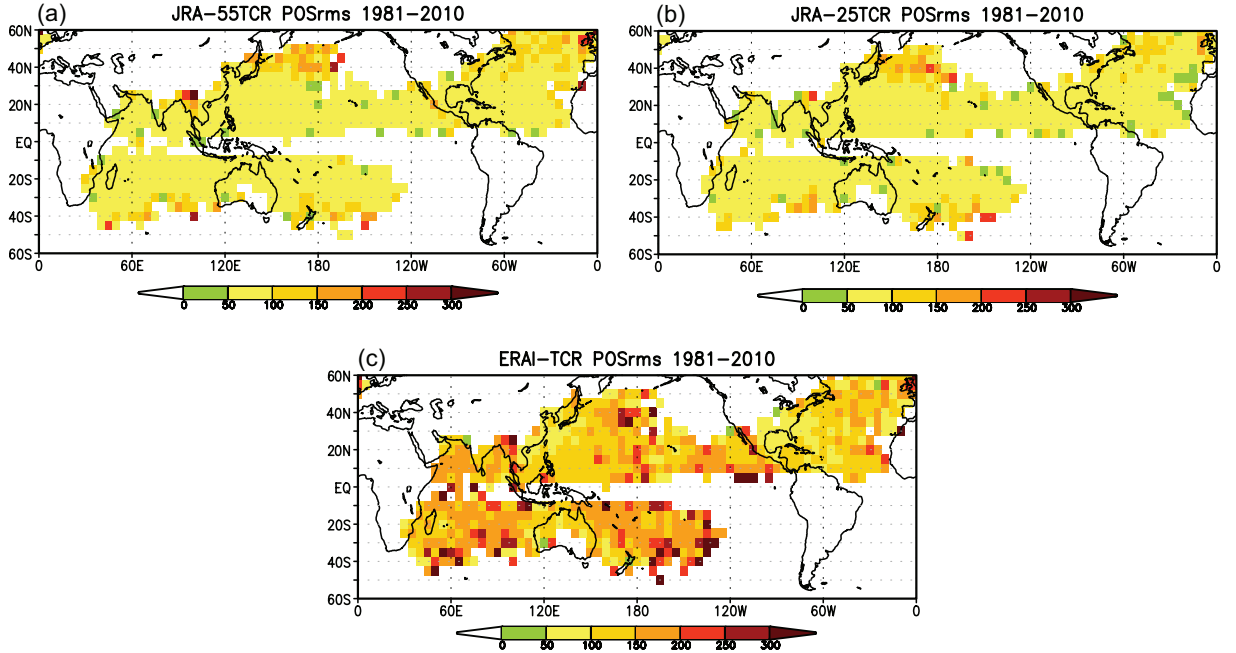


Fig. 11. Geographical distribution of the RMSE of TC position (km) with respect to the best track TC position in (a) JRA-55, (b) JRA-25, and (c) ERA-Interim averaged from 1981 to 2010.

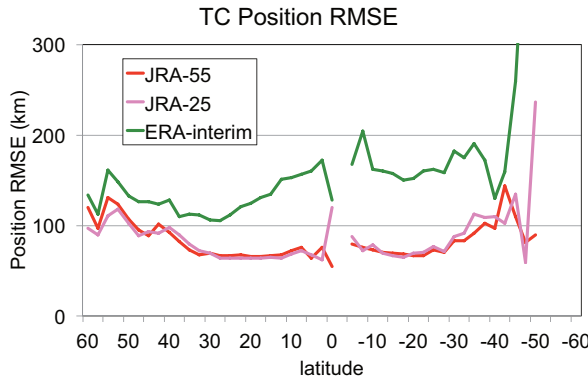


Fig. 12. Zonal mean of the RMSE of TC position difference for JRA-55, JRA-25, and ERA-Interim.

averaging weight is larger for TCs with the larger position error in the case of the RMSE, the magnitude of the TC position error tends to be highlighted in the large position error area for the RSME than for the mean distance.

In Fig. 11, the RMSE is smaller than 100 km in most areas in both JRA-55 and JRA-25. The grid spacing of the JRA-55 and JRA-25 products used

in this study is 1.25° ; hence, the RMSEs for the TC positions in JRA-55 and JRA-25 are less than the grid spacing in most areas. Thus, the TC position errors in JRA-55 and JRA-25 are negligible compared with the grid resolution, except at higher latitudes. TCs move faster at high latitudes than at low latitudes, meaning that the RSME is larger. Indeed, in the three reanalyses, large RMSEs are evident in the northeast sectors of the western North Pacific and the North Atlantic basins where most TCs undergo transitions to extra-tropical cyclones and move with higher speeds.

In ERA-Interim, the RMSE distribution is qualitatively similar to those in JRA-55 and JRA-25. In the extra-tropics of the western North Pacific and the North Atlantic, the magnitudes of the RMSE at most grid points are smaller than the 150 km grid spacing of the ERA-Interim product used in this study. The RMSEs in the northeast sector of the basins are much larger than the grid spacing, with values greater than 300 km at some grid points. On the other hand, RMSEs larger than the grid spacing are evident in the tropics and the SH (Figs. 11c, 12, respectively). The larger RMSE in ERA-Interim is thought to be related to the geographical distribution of the observational data. In the NH extra-tropics, more accurate TC representation is achieved due to the dense distribution of

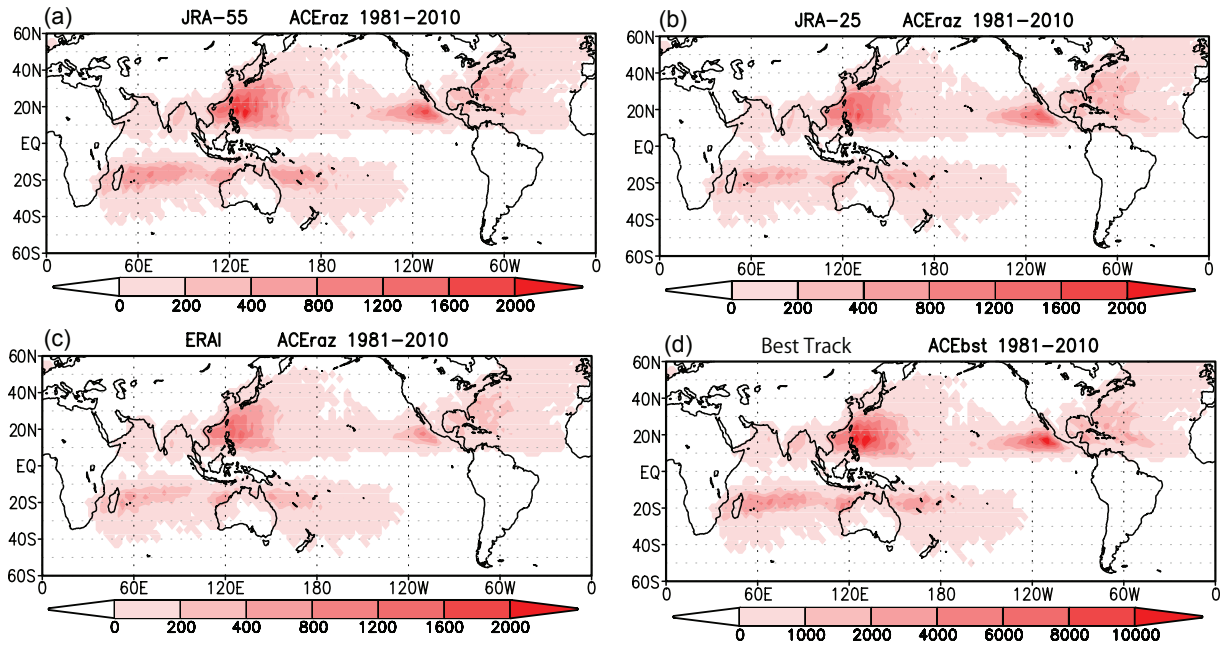


Fig. 13. Geographical distributions of ACE ($\text{m}^2 \text{s}^{-2}$) in (a) JRA-55, (b) JRA-25, (c) ERA-Interim, and (d) best track. Note that different color scales are utilized for reanalyses and the best track.

observational data, and a smaller position error from the best track is also expected. In the tropics and SH, however, the representation of TCs is relatively poor and their position errors also become large due to the scarcity of observations. In JRA-55 and JRA-25, comparable TC position errors are evident in both hemispheres due to the utilization of TCRs, even in areas with sparse observations. In JRA-25 and ERA-Interim, there are high RMSE spikes around 45°S. This error consists of only one grid point containing a small number of TCs; therefore, we can consider that these are exceptional cases. In TC analysis and modeling studies using reanalysis products, the exact TC position is often required, and large position errors are a serious problem. Schenkel and Hart (2012) showed the superiority of the TC position error in JRA-25 and CFSR, which introduce artificial TC manipulation, compared with those in other reanalyses without TC manipulation. Our results with less TC position error in JRA-55 support their results.

We evaluate the TC intensity as another aspect of TC representation. Here, we utilize accumulated cyclone energy (ACE) (Bell et al. 2000) as the measure of TC intensity, which is defined as the simple accumulation of the TC maximum wind speed squared in a 6-hour interval, which indicates the wind

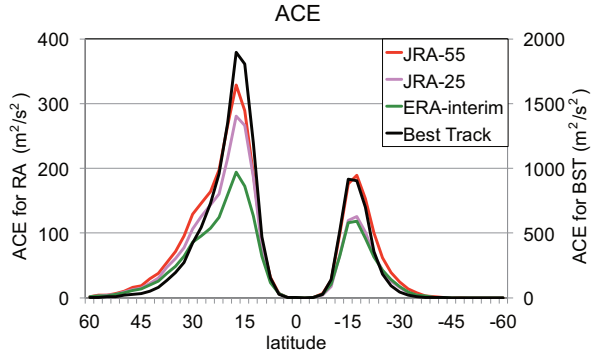


Fig. 14. Zonal mean ACEs from JRA-55, JRA-25, ERA-Interim, and the best track.

energy due to TCs. The ACE is measured in units of kt^2 in its original form, but we use units of $\text{m}^2 \text{s}^{-2}$. Figures 13 and 14 show the geographical distribution and zonal mean of ACE for JRA-55, JRA-25, ERA-Interim, and the best track. Note that in these figures the scale used for the reanalyses is different from that used for the best track because of the large differences between their ACEs. It should be noted that the TC intensities in reanalyses are generally weak compared with those observed due to a coarse

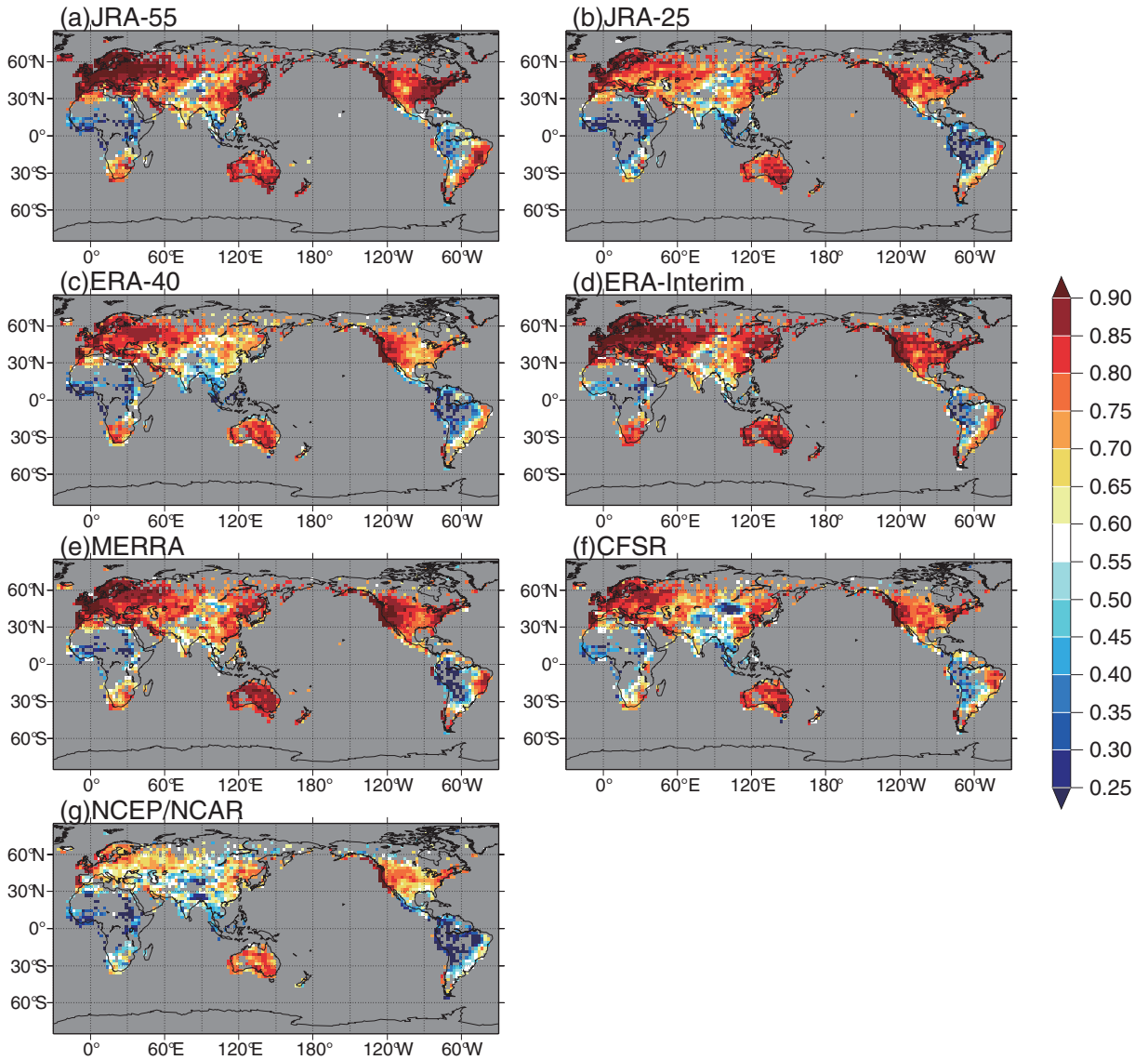


Fig. 15. Temporal correlation coefficients of monthly mean precipitation anomaly with GPCC for (a) JRA-55, (b) JRA-25, (c) ERA-40, (d) ERA-Interim, (e) MERRA, (f) CFSR, and (g) NCEP/NCAR reanalysis from 1980 to 2001. Temporal correlation coefficients are shown only for grid boxes in which rain gauge stations are present within corresponding areas for more than 80 % of the analyzed time period.

model resolution that does not resolve the inner structures of TCs. Figure 13 shows the qualitatively similar geographical distributions of the ACEs of the three reanalyses and the best track. The relatively large ACEs are located to the east of the Philippines and to the west of Mexico for the North Pacific, and in the area around Florida for the North Atlantic. In the SH, there is a zonal ACE maximum along 15–20°S. In the zonal mean shown in Fig. 14, the overall latitudinal

variation of ACEs in the reanalyses is similar to that in the best track. Of the three reanalyses, the largest ACE is observed in JRA-55, and the second largest in JRA-25, in the NH. The ratios of ACE north of 30°N to their maximum values in three reanalyses are relatively large compared with that of the best track; this implies that rapid intensification of TCs moving toward high latitudes is not properly analyzed. Further study regarding the reason for such TC behavior

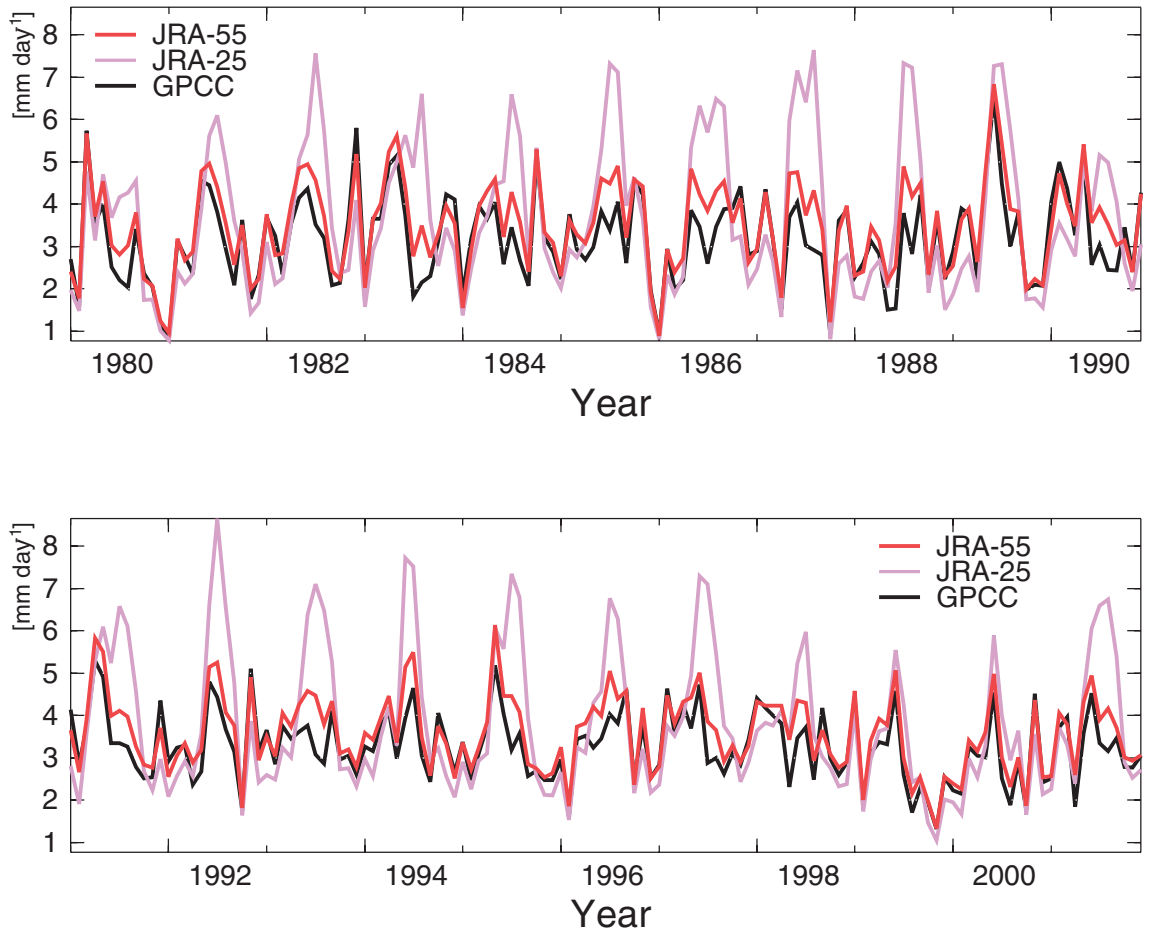


Fig. 16. Time series of monthly mean precipitation averaged over 30–40°N, 80–100°W.

would be necessary. Schenkel and Hart (2012) reported a northward shift in the TC maximum wind speed distributions in some reanalyses, including JRA-25 and ERA-Interim, compared with that of the best track. The relatively large ACE north of 30°N is considered to reflect a similar tendency in the location of the maximum wind speed found in the reanalyses. This topic needs to be improved in future reanalyses.

5. Climate variability in the extra-tropics

5.1 Precipitation over land

As described in Section 4.1, Kobayashi et al. (2015) compared global precipitation with the GPCP produced using both satellite data and surface rain gauge data. However, over land, the reliability of satellite-derived precipitation data is lower than it is

over the ocean (Nicholson et al. 2003a, b). Therefore, in this section, the performance and representation of JRA-55 for precipitation over extra-tropical land are described using GPCC data (Schneider et al. 2011; see also Section 2.2).

Figure 15 shows the distribution of the temporal correlation coefficient between the reanalyses and monthly mean precipitation obtained using GPCC data from 1980 to 2001. Note that temporal correlation coefficients are calculated only for grid boxes in which the rain gauge stations are present within the corresponding area for more than 80 % of the period. Areas of low correlation commonly appear in the tropics, for example, Central Africa, and the Amazon. However, these panels also indicate that the reanalyses yield more accurate precipitation data over land

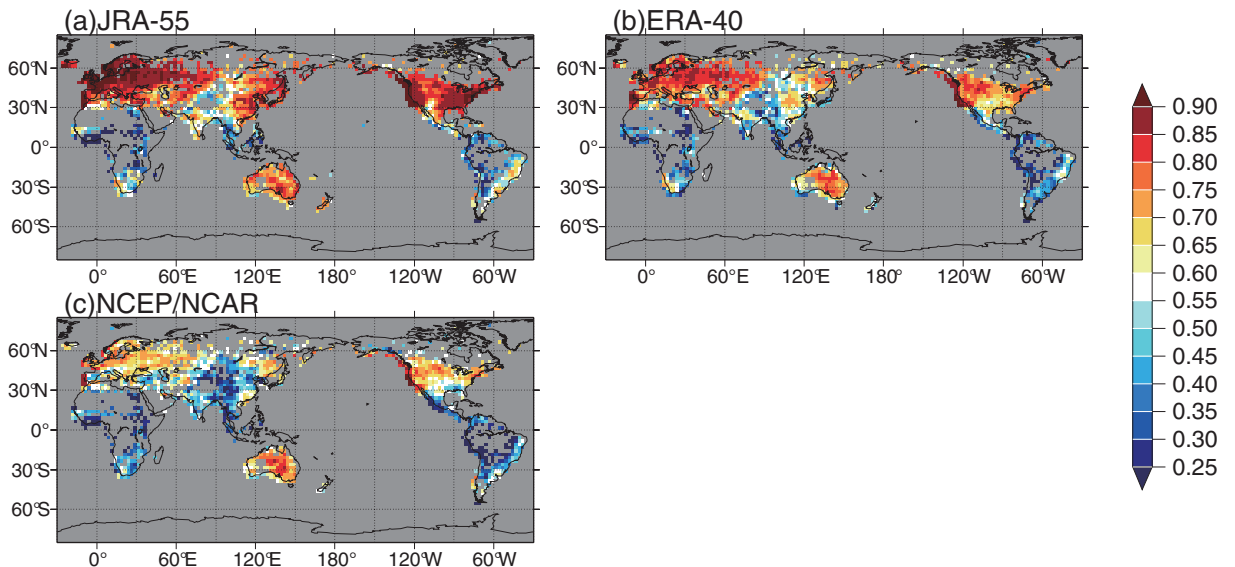


Fig. 17. As in Fig. 15, but from 1958 to 1979 for (a) JRA-55, (b) ERA-40, and (c) NCEP/NCAR reanalysis.

in the NH extra-tropics. Furthermore, JRA-55 (Fig. 15a) is superior to JRA-25 (Fig. 15b), ERA-40 (Fig. 15c), MERRA (Fig. 15e), and CFSR (Fig. 15f) in regions such as Europe, Russia, southeastern North America, and around Brazil, and is approximately comparable to ERA-Interim (Fig. 15d); in particular, improvements in southeastern North America and around Brazil in JRA-55 from JRA-25 are noteworthy. The exclusion of surface pressure observations over the Amazon basin in JRA-55 is related to the improvements around Brazil, as described in Section 7.2 of Kobayashi et al. (2015).

Figure 16 shows time series of monthly mean precipitation data averaged over 30–40°N, 80–100°W, corresponding to southeastern North America. JRA-25 tends to overestimate the precipitation in this area during the warm season, resulting in a lower temporal correlation with the GPCC data. The precipitation estimated by JRA-55 is satisfactorily consistent with the GPCC results.

Figure 17 illustrates the distribution of the temporal correlation coefficient between the reanalyses and monthly mean precipitation obtained using GPCC data from 1958 to 1979. JRA-55 exhibits higher correlation coefficients over Eurasia and North America compared with those of ERA-40 and the NCEP/NCAR reanalysis. This result indicates that the representation of precipitation over extra-tropical land in JRA-55 is of high quality throughout the reanalysis

period.

5.2 Comparison of storm tracks

In the extra-tropics, synoptic-scale cyclones play an important role in providing the momentum flux to sustain mid-latitude large-scale circulation. We refer to synoptic-scale cyclones as transient eddies, in contrast to stationary Rossby waves. Transient eddies develop along SST fronts, where the main regions of the tracks of extra-tropical disturbances are formed (Nakamura et al. 2008, Sampe et al. 2010). Compo et al. (2011) compared the synoptic variabilities in the storm track regions and found weaker variabilities where observations were sparse. Here, we describe the representation of transient eddies in the extra-tropics in JRA-55, focusing on the effect of changing the observing system on the synoptic variability in the storm track regions in JRA-55.

Figure 18 shows 2–8-day band-pass-filtered transient eddy kinetic energies (KEs) at the 300 hPa level during the NH cold season (November–March) from 1980/1981 to 2000/2001. Two regions of maximum KE are observable in the North Pacific and the North Atlantic, and all reanalyses succeed in qualitatively representing these regions. However, the North Pacific KEs in JRA-25, ERA-40, and the NCEP/NCAR reanalyses are clearly lower than those in ERA-Interim. The KE in JRA-55 is also slightly lower than that in ERA-Interim but it is stronger than

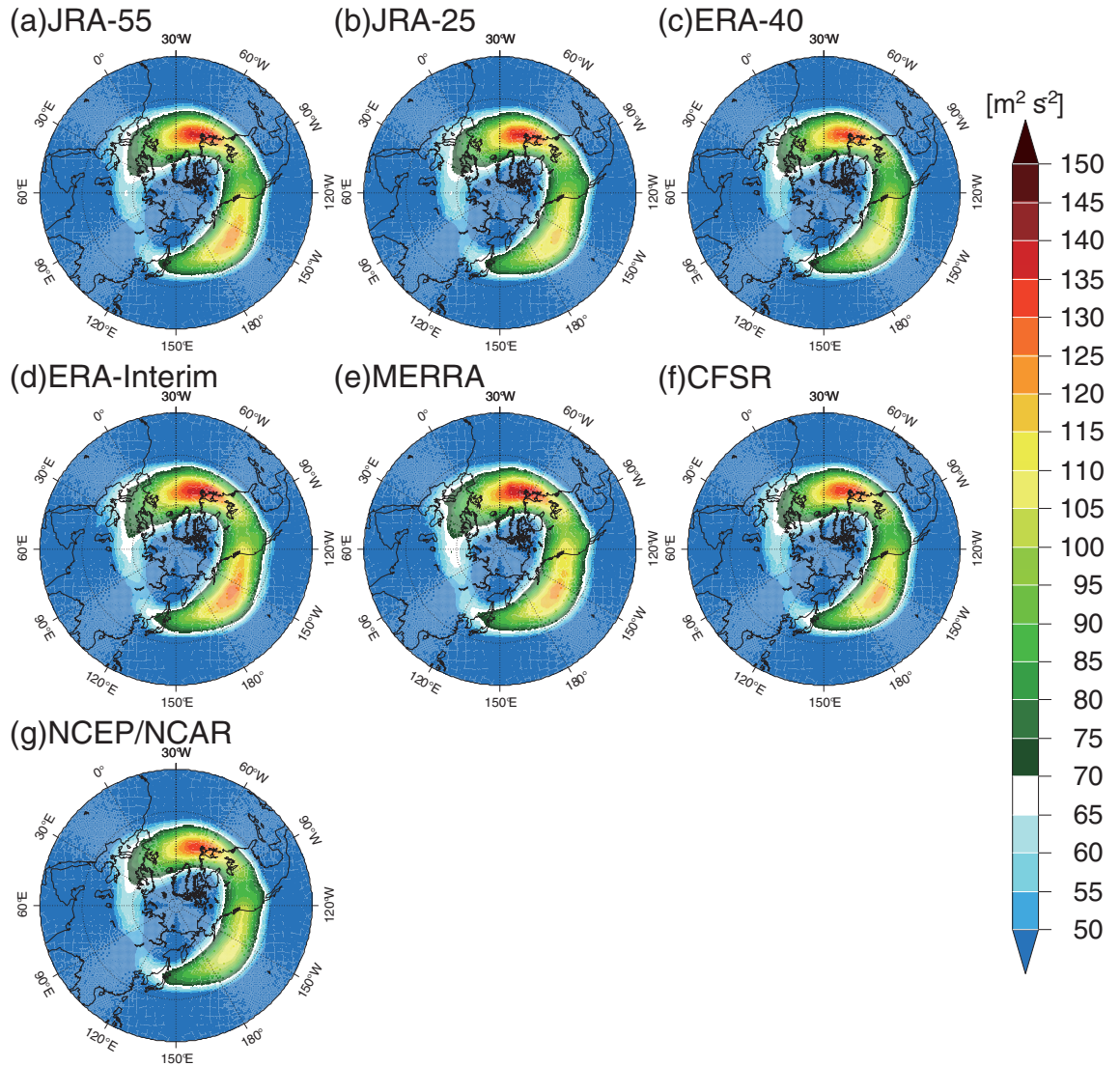


Fig. 18. Band-pass-filtered 2–8 day transient eddy KEs at 300 hPa level during NH cold season (November–March) from 1980/1981 to 2000/2001 for (a) JRA-55, (b) JRA-25, (c) ERA-40, (d) ERA-Interim, (e) MERRA, (f) CFSR, and (g) NCEP/NCAR reanalysis.

the KEs in the other reanalyses. Moreover, during the NH cold seasons from 1958/1959 to 1979/1980, the KE in ERA-40 is quite weak compared with its values after 1980/1981 (Fig. 19). Although the KE in JRA-55 is also weaker, it is much stronger than those in the ERA-40 and NCEP/NCAR reanalyses. These results indicate that JRA-55 is not much affected by changes in the observation system on the representation of storm tracks. Furthermore, JRA-55 improves the temporal consistency.

In order to assess the representations of storm

tracks, we conducted an investigation using band-pass-filtered daily mean OLR. The development of transient eddies is closely related to the distribution of developed clouds. Hence, it is necessary to assess not only the KEs of transient eddies but also the distributions of developed clouds that correspond to areas of lower OLR in the mid-latitudes. Figure 20 shows the frequencies of the spatial correlations of 2–8 day band-pass-filtered daily mean OLRs over the storm track regions with NOAA OLR during the NH cold seasons from 1980/1981 to 2000/2001.

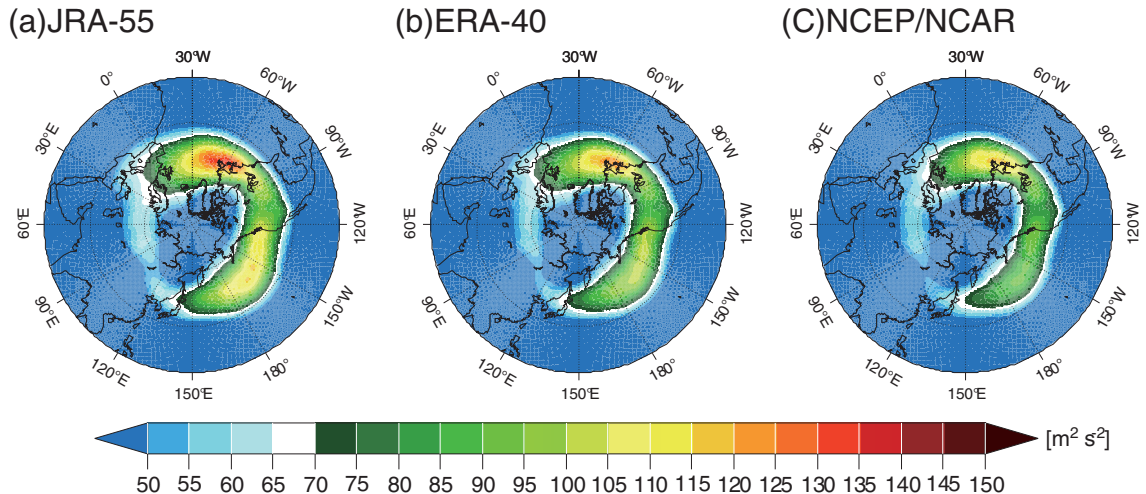


Fig. 19. As in Fig. 18, but during the NH cold season from 1959/1960 to 1979/1980 for (a) JRA-55, (b) ERA-40, and (c) NCEP/NCAR reanalysis.

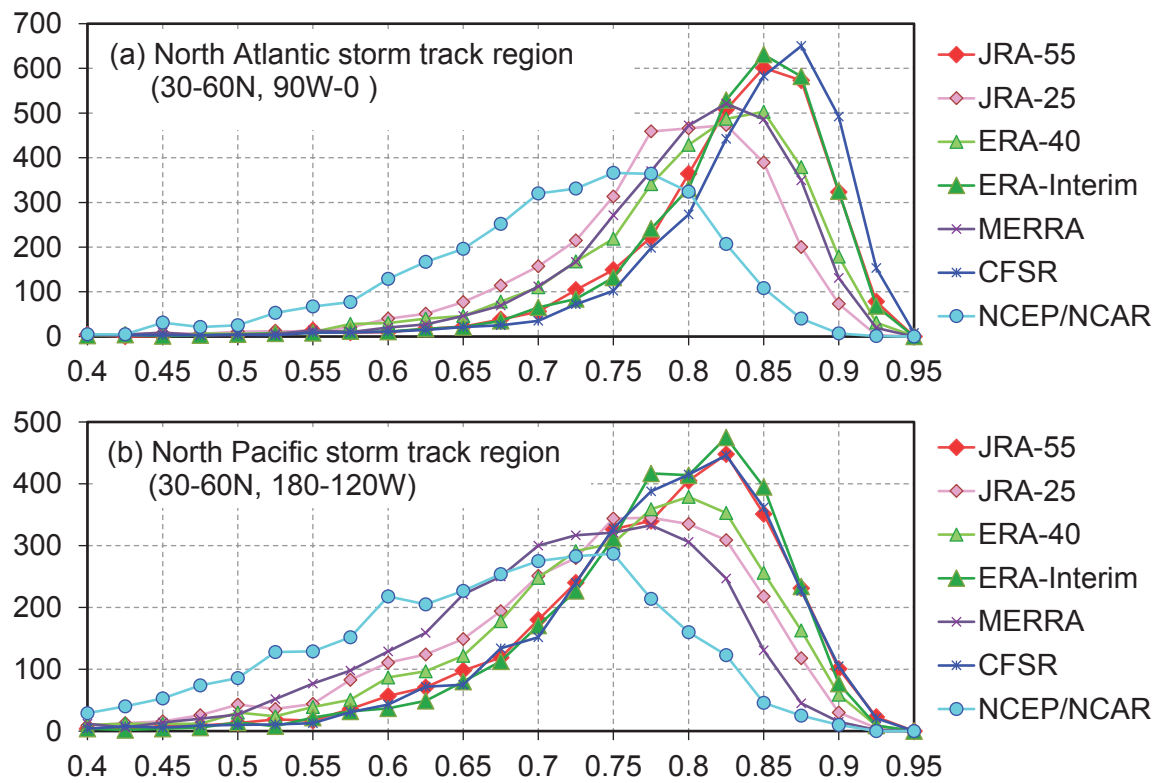


Fig. 20. Frequency of spatial correlation of 2–8 day band-pass-filtered daily mean OLR over storm track regions with NOAA OLR during NH cold season (November–March) from 1980/1981 to 2000/2001 for (a) North Atlantic and (b) the North Pacific storm track regions, respectively.

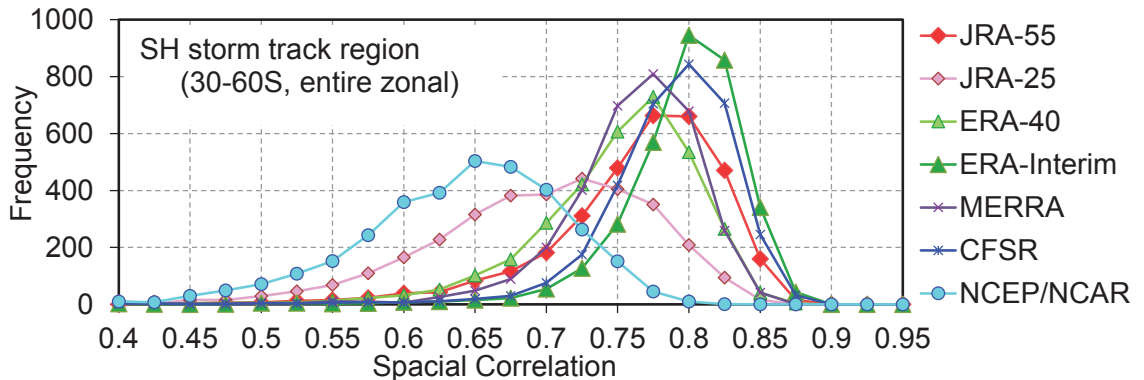


Fig. 21. As in Fig. 20, but for SH storm track region ($30\text{--}60^{\circ}\text{S}$, entire zonal) during the SH cold season (May–September) from 1980 to 2001.

Clearly, high spatial correlation coefficients in both the North Atlantic and the North Pacific are more frequent in JRA-55 (red diamonds), CFSR (blue crosses), and ERA-Interim (green triangles) than in MERRA (purple crosses), ERA-40 (right green triangles), and JRA-25 (pink diamonds). In particular, low spatial correlation coefficients in the North Atlantic storm track region are less frequent in JRA-55 than in JRA-25 (Fig. 20a), indicating that JRA-55 greatly improves the representation of each transient eddy from JRA-25 in this region. In the SH cold season (Fig. 21), the qualities of ERA-Interim and CFSR are outstanding, while JRA-55 is not as good as these two reanalyses. However, it clearly improves upon the representation of each transient eddy from JRA-25, as in the North Atlantic.

5.3 Siberian High

In the NH winter, the Siberian High develops in northeastern Eurasia in association with the accumulation of an extremely cold air mass. Cold air outbreaks from the Siberian High greatly influence the climates of East Asia and Europe, and even that of Southeast Asia. Here we focus on SLP over Eurasia in boreal winter, which is used to measure the intensity of the Siberian High.

Figure 22 shows the distributions of SLP during the NH winter (December–February) from 1980/1981 to 2000/2001 in the observational dataset HadSLP2 (Allan and Ansell 2006) and in that subtracted from each of the reanalysis products. The SLP in northeastern Eurasia is the highest in the NH (Fig. 22a), and all reanalyses have a distinct negative bias in northeastern Eurasia (Figs. 29b–h). Clearly, JRA-55

(Fig. 22b) reduces the negative bias in this region compared with JRA-25 (Fig. 22c). Figure 23 shows time series of NH winter mean SLP averaged over $40\text{--}60^{\circ}\text{N}$, $80\text{--}120^{\circ}\text{E}$, corresponding to the area of the Siberian High. The long-term trend of JRA-55 (red line in Fig. 23) is not very different from that of HadSLP2. On the other hand, ERA-40 exhibits much higher SLP values before 1979 than during the subsequent period, resulting in a marked negative trend for the whole period. Although reanalyses are generally consistent after 1980, except for MERRA, which yields assignable negative bias in this region throughout the period, differences from HadSLP2 are observable. In addition, JRA-25 exhibits lower values in the 1980s. JRA-25 has larger SLP analysis increments during 1979–1988 compared with the period after 1989 (Fig. 24). We excluded large negative biased surface pressure observations from Mongolian stations, which resulted in a successful reduction of inappropriate analysis increments.

6. Climate variability in the stratosphere

6.1 Stratospheric temperature

Kobayashi et al. (2015) compared monthly temperature anomalies from reanalyses with independent observational datasets for the layers from the lower stratosphere to the top of the stratosphere. In this section, we discuss the features on a regional basis. Figure 25 shows time series of regionally averaged 30-hPa-level temperature deviations from the climatological mean for the period from 1981 to 2001. In the extra-tropical stratosphere during the NH winter (Fig. 25a), the inter-annual variability of the reanalyses is approximately consistent. In the tropics

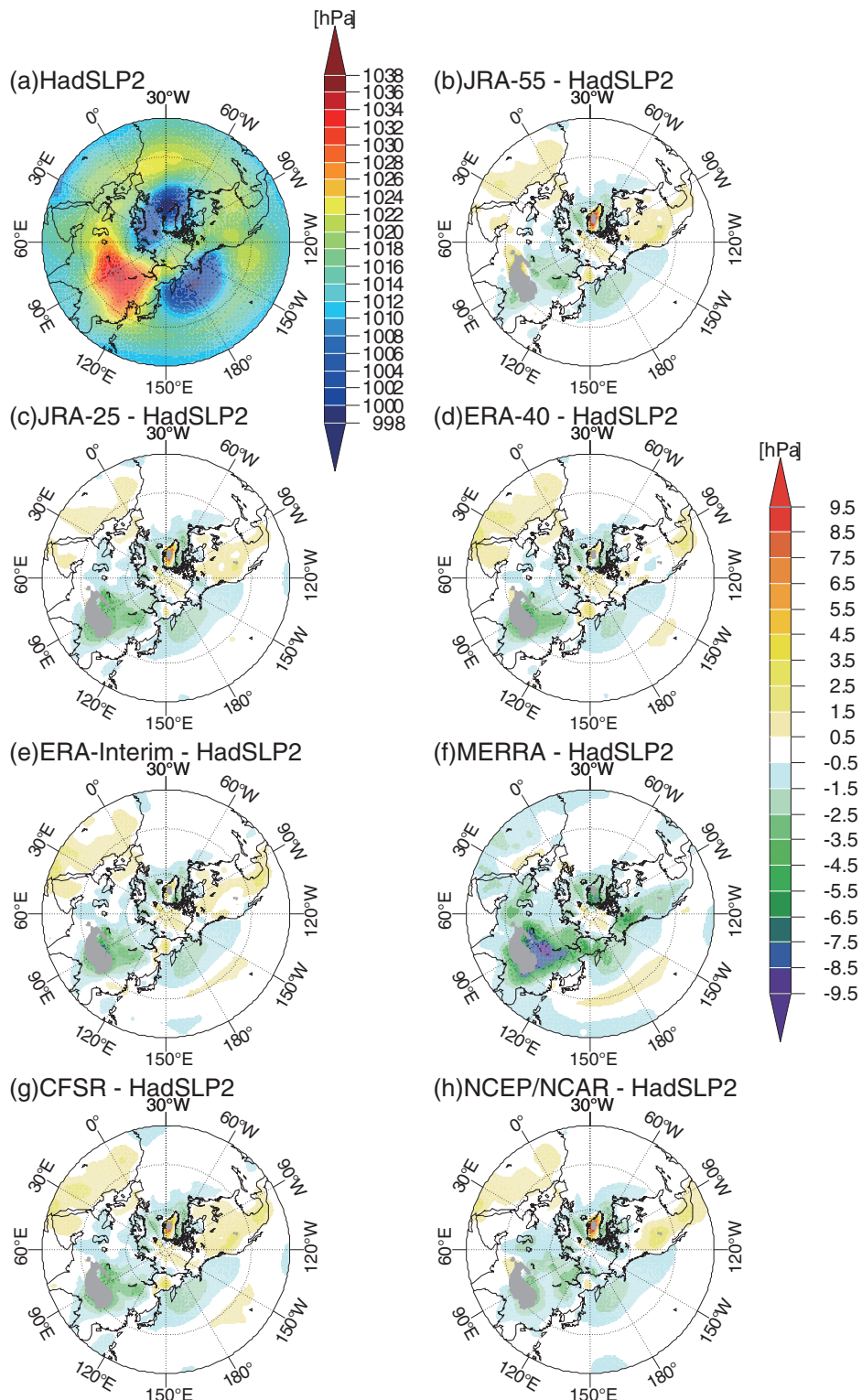


Fig. 22. Distributions of (a) SLP (hPa) from HadSLP2 and (b–h) that subtracted from each reanalysis product during NH winter (December–February) from 1980/1981 to 2000/2001. Gray shadings indicate areas with altitudes exceeding 3000 m.

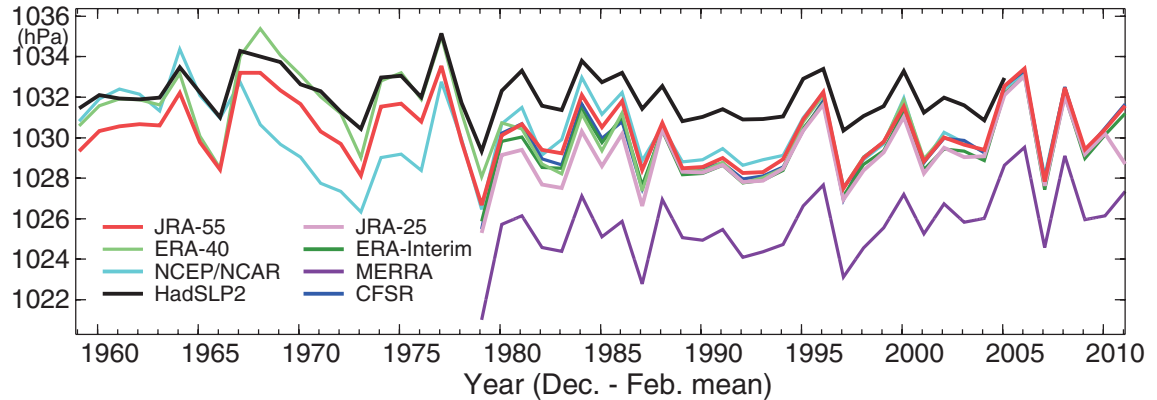


Fig. 23. Time series of NH winter (December–February) mean SLP (hPa) averaged over 40–60°N, 80–120°E.

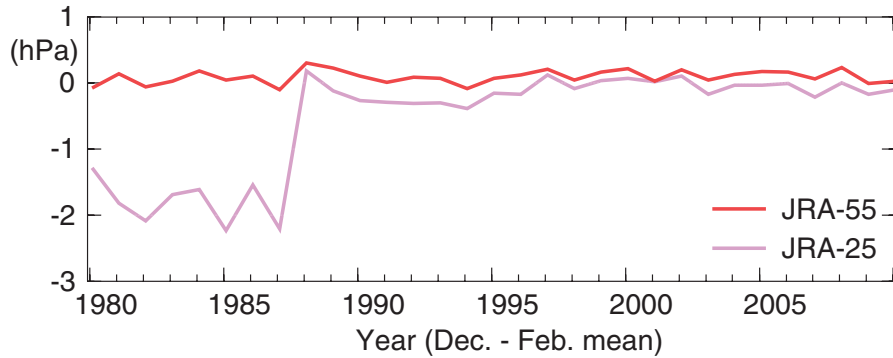


Fig. 24. Time series of winter (December–February) mean SLP analysis increments (hPa) averaged over 45–55°N, 90–105°E.

(Fig. 25b), the reanalyses are also comparable except for JRA-25, which exhibits an artificial jump in 1998. Kobayashi et al. (2015) reported that the forecast model used in JRA-25 had a significant cold bias in the lower stratosphere, causing difficulty in correcting the bias due to satellite radiances and resulting in some discontinuity in the analysis in response to changes in observing systems or bias correction methods for satellite radiances. JRA-55 succeeded in reducing such discontinuous changes considerably. At high latitudes in the stratosphere during the SH winter (Fig. 25c), larger discrepancies between the reanalyses are observable before 1979. The temperature anomalies of ERA-40 are much colder than those of JRA-55 in this period.

Figure 26 compares the reanalyses with radiosonde observations that passed quality control checks in the JRA-55 system at the 30 hPa level over New Zealand

in the SH winter (June–August) 1963. We selected the observational points, which are the southernmost available radiosonde observations. ERA-40 seems to have a cold bias at this level. Uppala et al. (2005) pointed out a pronounced (~ 10 K) cold bias in winter and springtime analyses in the Antarctic lower stratosphere in the early years; this is evident from comparison with later ERA-40 analyses and other climatologies. The result above is consistent with this finding.

Figure 27 illustrates the results of a comparison of retrieved temperatures from Aura MLS (Waters et al. 2006; see also Section 2.2). The details of the comparison method are described in Section 2.3. In the upper stratosphere, JRA-25 has a cold bias around 5 hPa in the NH and a warm bias just above this level (Fig. 27c). Although JRA-55 has reduced biases in the lower stratosphere compared with JRA-25 (Fig. 27b), it has a large warm bias in the lower meso-

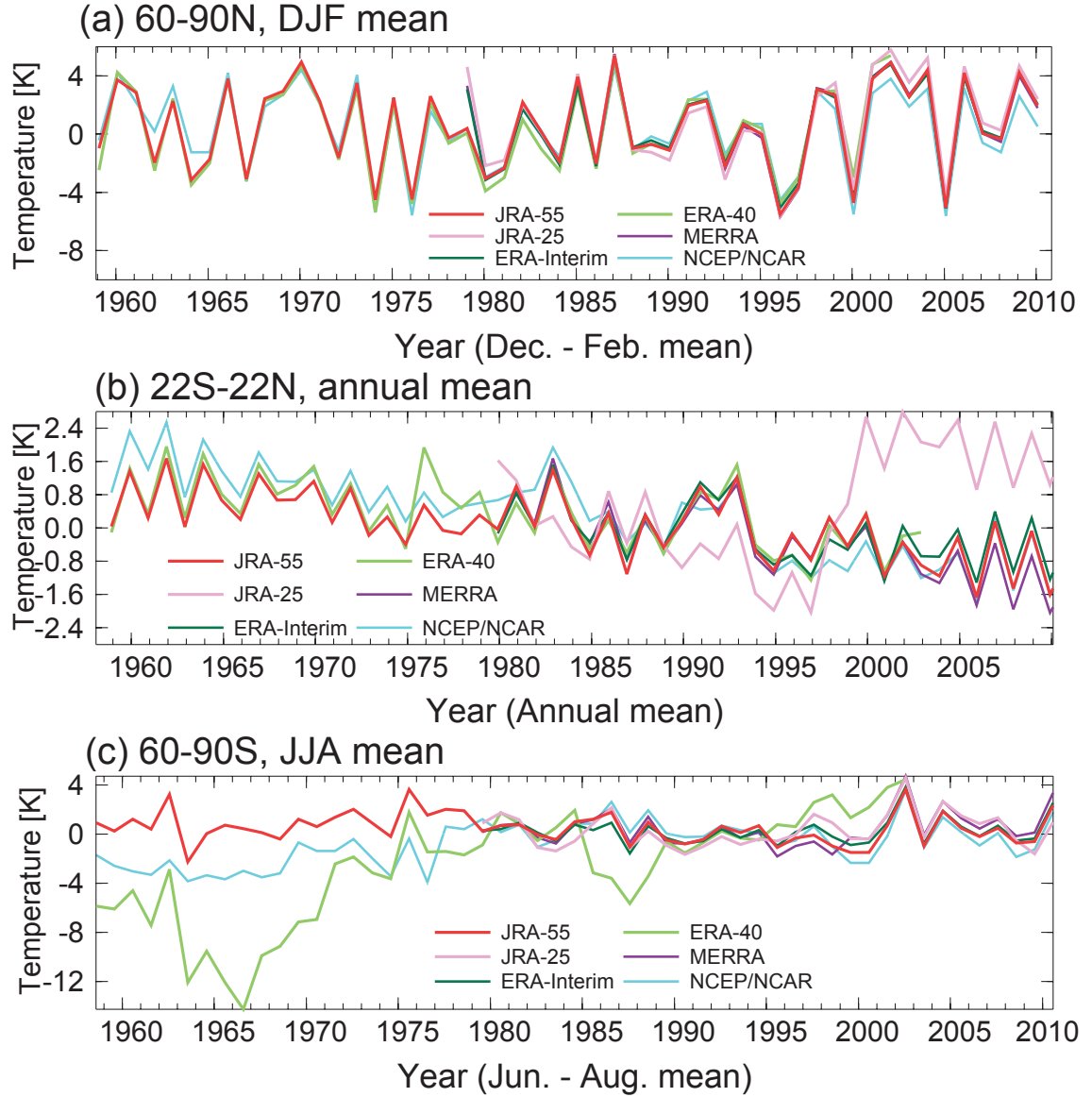


Fig. 25. Time series of 30-hPa-level temperature deviations (K) from climatological mean from 1981 to 2001, averaged over (a) 60–90°N, NH winter (December–February), (b) 22°S–22°N annual mean, and (c) 60–90°S, SH winter (June–August).

sphere (above 1 hPa) except in the polar region of the NH. MERRA does not have any large biases except around the stratopause and above, and ERA-Interim has a smaller bias profile than the other reanalyses generally. These features indicate that these reanalyses improve the representation of stratospheric temperature, although large uncertainties still exist in and around the stratopause and above.

6.2 Sudden Stratospheric warming in the Northern Hemisphere

SSW is a phenomenon with a hemispheric spatial scale but a short timescale in the winter stratosphere, causing the polar stratospheric temperature to increase by more than 25 K within a week. To represent SSW events more precisely, it is important to make use of as many upper-air observations as possible. However, during the pre-satellite era (before 1979), radiosondes

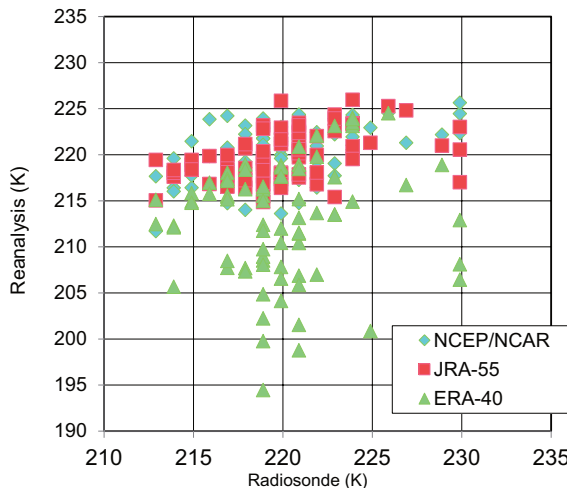


Fig. 26. Scatter diagram showing radiosonde temperatures at 30 hPa from stations at Invercargill (New Zealand) and Campbell Island (New Zealand), and values at the analysis grid points nearest to these locations, during the SH winter (June–August) 1963. Only quality-controlled radiosonde observations are plotted.

were the only upper-air observing system and radiosonde observations were sparse in the polar region, making it difficult to represent SSW events during this period.

Figure 28 shows time series of temperature at 30 hPa averaged over 60–90°N in the NH winter of 1962/1963. In January 1963, a wave-2-type major SSW occurred in the NH (Finger and Teweles 1964). The rapid increase in temperature is observable in the second half of January 1963, with the temperature peaking at the beginning of February 1963. At this peak, ERA-40 yields the highest temperature among the three reanalyses. JRA-55 is a few degrees lower than ERA-40 at the peak but is comparable in other periods. On the other hand, the NCEP/NCAR reanalysis is not consistent with ERA-40 and JRA-55. It tends to be warmer before the SSW and colder than the others around the peak of the warming.

Figure 29 compares the reanalyses with radiosonde observations at the 30 hPa level in Canada (red star and diamond in Fig. 30a mark the locations of radiosonde observations). Evidently, ERA-40 fits the radiosonde observations well over the entire temperature range, while JRA-55 has a cold bias for temperatures above 220 K. The NCEP/NCAR reanalysis also seems to have a cold bias for temperatures above 220

K and a warm bias below 210 K. These features may be related to the weak amplitude of planetary waves with zonal wavenumber 2 in the numerical prediction model.

Figure 30 shows the 30 hPa geopotential heights of the reanalyses on 31 January 1963 at 00 UTC. At the peak of the warming, two ridges develop over the North Atlantic and the Kamchatka Peninsula, and the polar vortex splits. One of the polar vortices shifts over Novaya Zemlya. JRA-55 and ERA-40 represent these features and resemble each other. On the other hand, in the NCEP/NCAR reanalysis, the development of the two ridges is weaker and the polar vortex over Novaya Zemlya is stronger than it is in the other reanalyses. These results suggest that the representation of SSW events in these reanalyses contains uncertainty during the pre-satellite era.

6.3 Equatorial stratosphere

The quasi-biennial oscillation (QBO) is a quasi-periodic oscillation of the zonal wind between easterly and westerly flow and is a robust phenomenon in the equatorial lower stratosphere (Ebdon 1960). The stratospheric semi-annual oscillation (SSAO) is dominant in the equatorial upper stratosphere (Reed 1965; Jones and Pyle 1984).

Figure 31 shows time–pressure cross-sections of the zonal-mean zonal wind component averaged over 5°S–5°N for the period from 1958 to 1978. JRA-55, ERA-40, and the NCEP/NCAR reanalysis well represent the general features of the QBO and SSAO. However, the scatter diagrams in Fig. 32 show that the correspondence between the reanalyses and the radiosonde observations before 1978 are not comparable to those after 1979 (not shown). In particular, the differences between the reanalyses and the radiosonde observations in the easterly phase at the 10 hPa and 30 hPa levels are very large. In addition, the reanalyses exhibit an easterly bias when radiosonde observations indicate a weak westerly phase, except for JRA-55 at the 70 hPa level. Such cases occur during westerly acceleration phase (eastward wind shear) (Fig. 33a). Westerly accelerations in the reanalyses are only about half of those in the radiosonde observations (Fig. 33b). Kawatani et al. (2010) pointed out that eastward equatorial waves including Kelvin waves contribute up to 25–50 % to driving the QBO in the eastward wind shear (westerly acceleration phase). The forecast model used in JRA-55 does not simulate QBO spontaneously (Kobayashi et al. 2014) because it does not use a non-orographic gravity wave drag parameterization. Therefore, the weak westerly

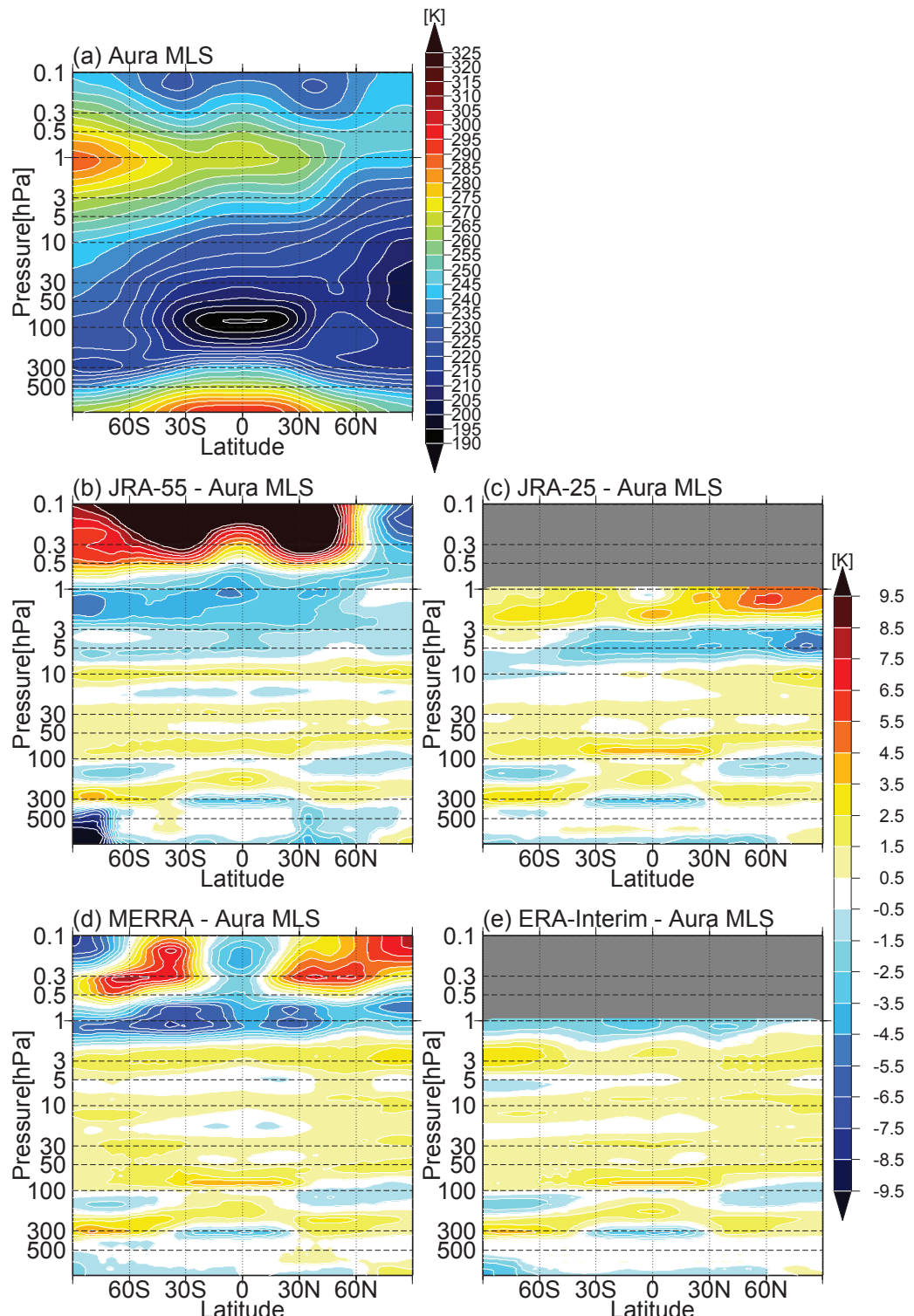


Fig. 27. Latitude-pressure cross-sections for (a) zonal mean Aura MLS temperature and (b–e) zonal mean temperature bias between reanalyses and Aura MLS during the NH winter (December–February) from 2005/2006 to 2011/2012.

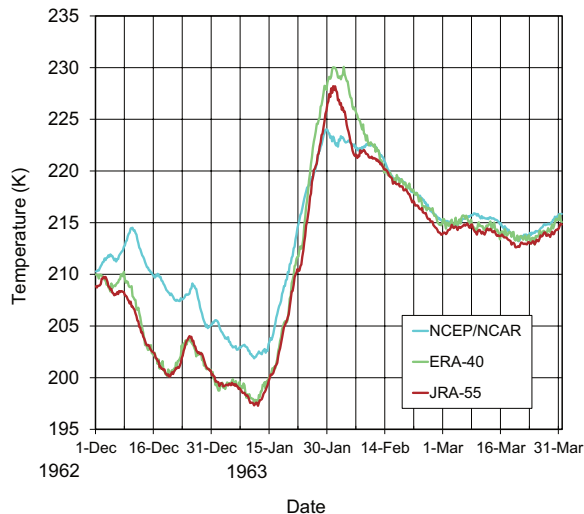


Fig. 28. Time series of temperature at 30 hPa averaged over 60–90°N in the NH winter of 1962/1963.

acceleration in the reanalyses may have been caused by the lack of non-orographic gravity wave drag parameterization and the weaker amplitude of equatorial waves before 1978, as described in Section 4.2. This issue requires further investigation.

7. Long-term trends in surface air temperature

Kobayashi et al. (2015) compared globally averaged land-surface air temperature anomalies from the Climate Research Unit (CRU) temperature database (CRUTEM4, Jones et al. 2012) with those of the NCEP/NCAR reanalyses, ERA-40, JRA-25, and JRA-55 and showed that the low-frequency variability of land-surface temperature anomalies in JRA-55 is reasonably similar to that in CRUTEM4 except for a difference of less than 0.1 K in warming after the 1990s. To further evaluate the surface air temperature accuracy of JRA-55, Fig. 34 compares the global distributions of long-term temperature trends in HadCRUT4 (Morange et al. 2012, see also Section 2.2), ERA-40, JRA-55, and the NCEP/NCAR reanalysis for the period from 1958 to 2001. The spatial distribution of the long-term temperature trend in JRA-55 seems to be the closest to that in HadCRUT4. To confirm this result quantitatively, the global means of the RMSE between the HadCRUT4 and reanalyses over land areas are calculated, and we found that the RMSE for JRA-55 is 0.0989 K decade⁻¹ and that it is smaller than the values for ERA-40 (0.129 K

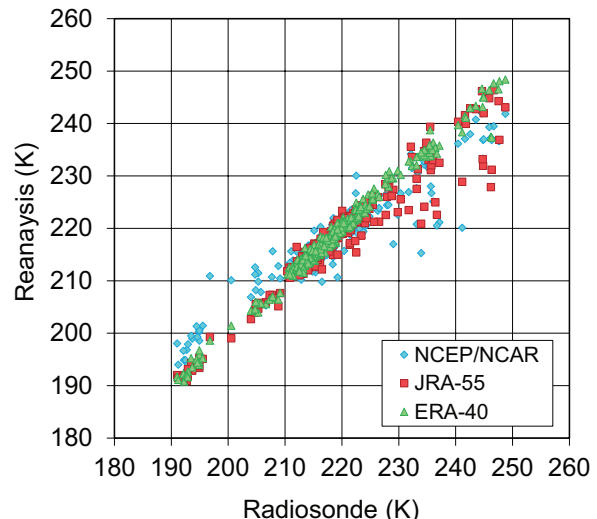


Fig. 29. Scatter diagram showing radiosonde temperatures at 30 hPa from stations at Norman Wells (Canada) and Resolute (Canada), and values at the analysis grid points nearest to these locations in the NH winter (December–February) of 1962/1963. Only quality-controlled radiosonde observations are plotted. Red star and diamond in Fig. 30a mark the locations of Norman Wells and Resolute, respectively.

decade⁻¹) and the NCEP/NCAR reanalysis (0.151 K decade⁻¹). The NCEP/NCAR reanalysis shows negative trends in the Sahara, around the Tibetan Plateau, and in Australia and western North America, which are inconsistent with HadCRUT4. In ERA-40, the negative trends in South America and Australia are large. JRA-55 also shows poor agreement with observations in southeastern Australia.

Figure 35 shows time series of SH winter mean surface temperature (K) averaged over 20–35°S, 140–155°E, corresponding to southeastern Australia. Before 1965, the analysis and 6-hour forecast (background) are consistent. However, after the 1970s, the difference between the analysis and the 6-hour forecast gradually increases, reaching about 1 K after the 1990s. We suppose that the difference is related to the change in the number of stations observing the surface air temperature in southeastern Australia. In Australia, the number of surface observations was less than 10 before 1965, which was not sufficient to correct the warm bias in background fields that originated in the forecast model used in JRA-55. As the number of surface observation stations has increased over time and reached 80 after 1978, the observations have

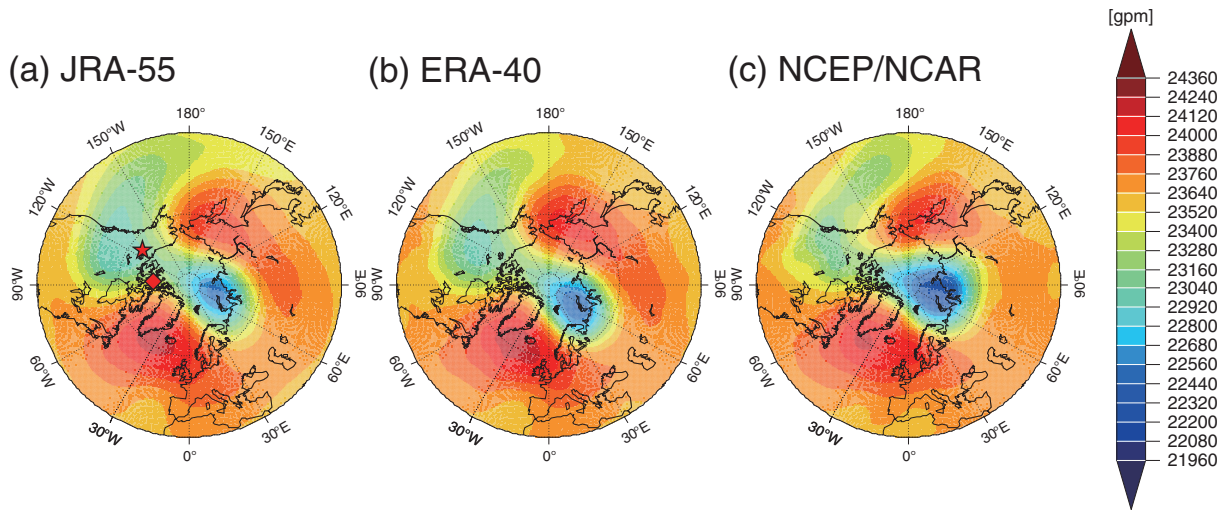


Fig. 30. Geopotential heights at 30 hPa (gpm) on 31 January 1963 at 0000 UTC in the NH for (a) JRA-55, (b) ERA-40, and (c) NCEP/NCAR reanalysis. Red star and diamond in (a) mark locations of Norman Wells and Resolute, respectively.

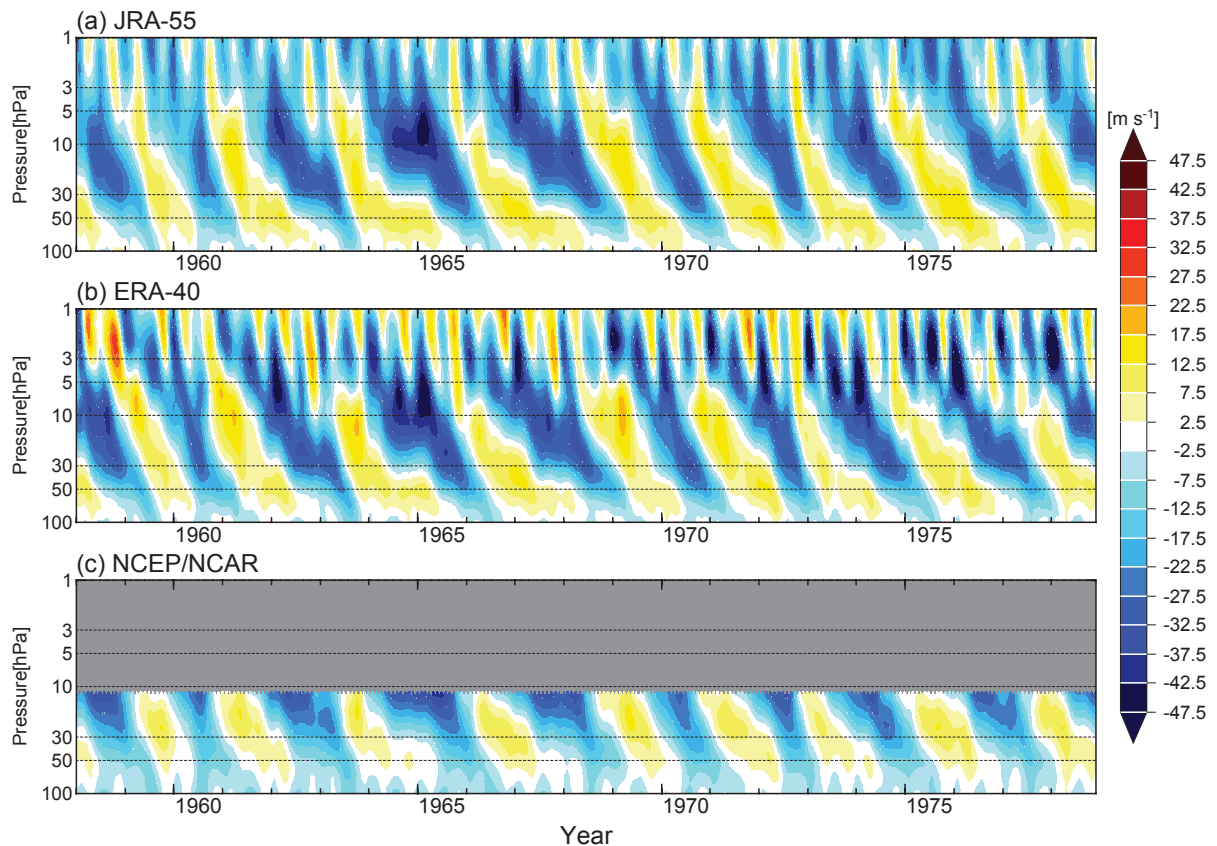


Fig. 31. Time–pressure cross-sections of the zonal-mean zonal wind component averaged over 5°S – 5°N from 1958 to 1978 for (a) JRA-55, (b) ERA-40, and (c) NCEP/NCAR reanalysis.

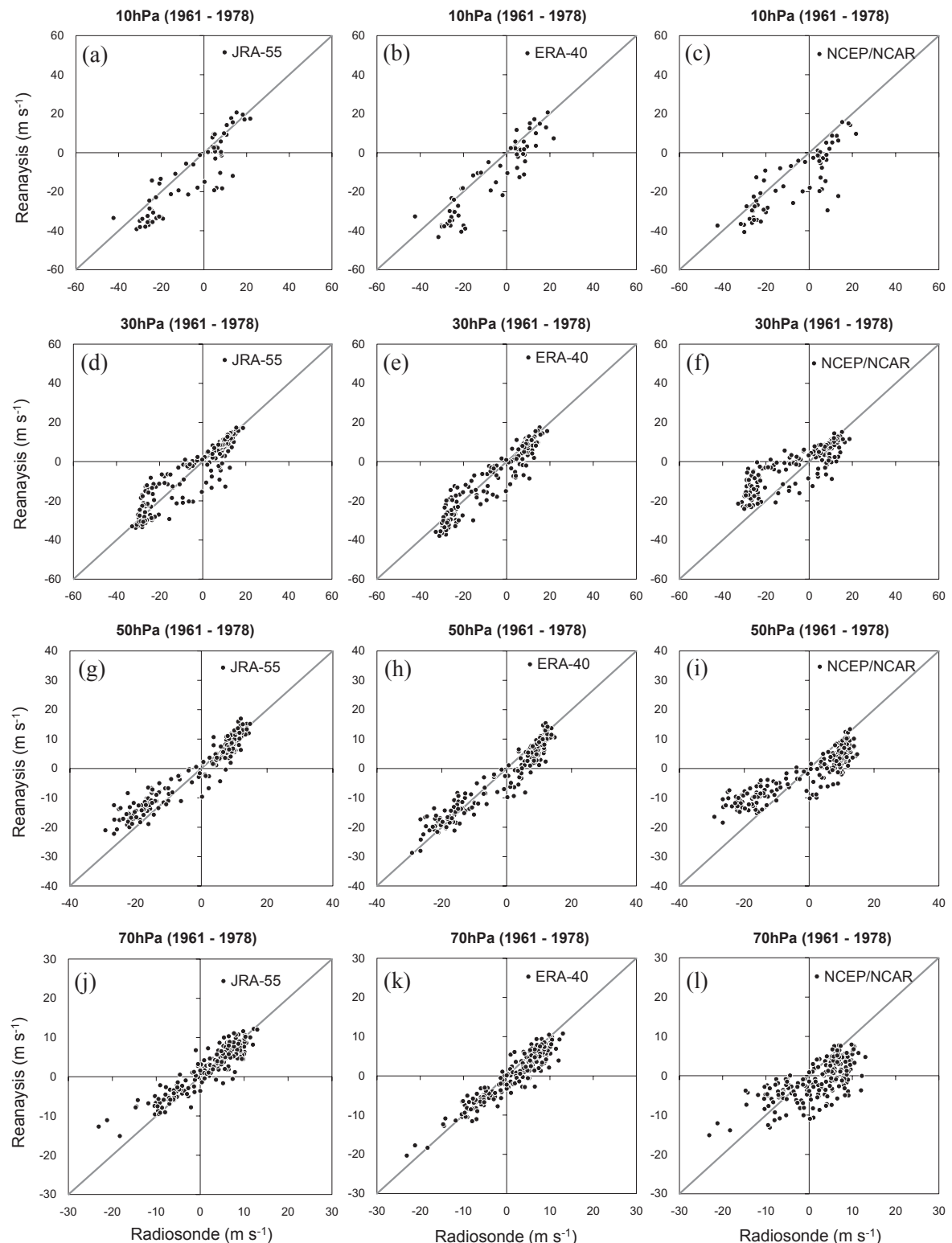


Fig. 32. Scatter diagrams showing monthly mean radiosonde zonal winds from the station at Singapore (x-axis) and analyses averaged over 0–2.5°N, 100–105°E (y-axis) from 1961 to 1978.

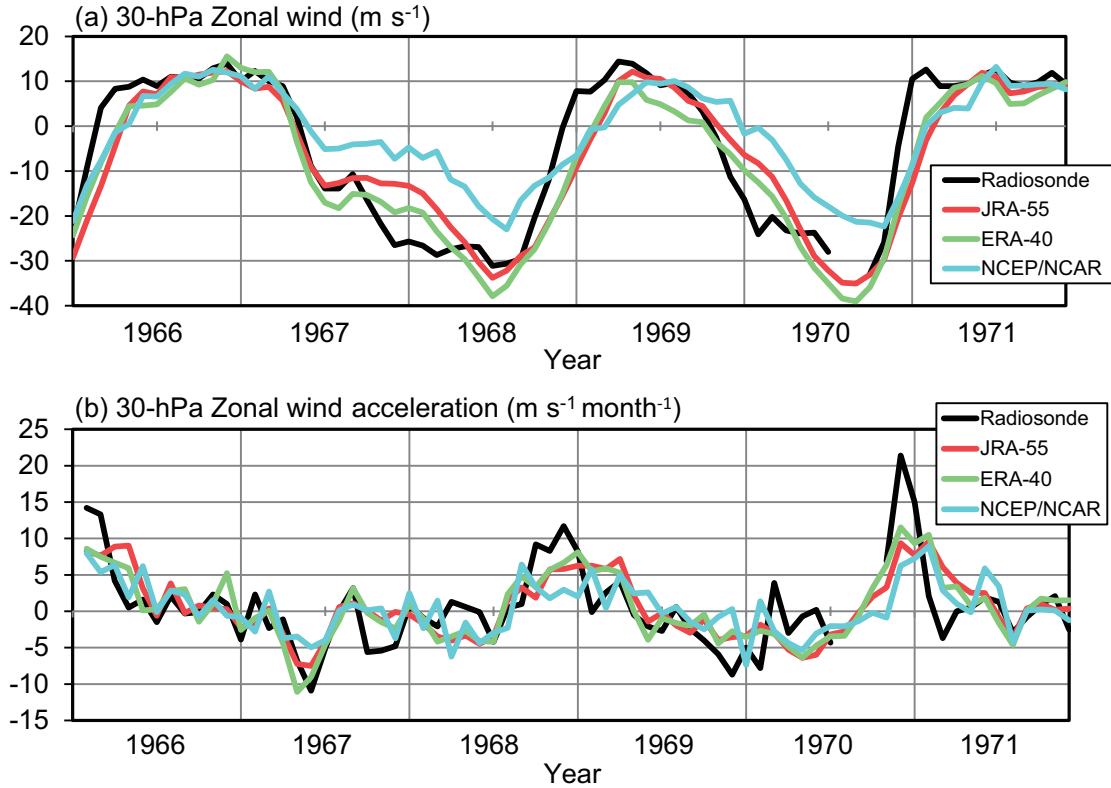


Fig. 33. Time series of (a) 30 hPa zonal wind component (m s^{-1}) and (b) its acceleration ($\text{m s}^{-1} \text{month}^{-1}$) for reanalyses and radiosonde observations from 1966 to 1971. Reanalyses are averaged over $0\text{--}2.5^\circ\text{N}$, $100\text{--}105^\circ\text{E}$, and radiosonde observations are from Singapore.

begun to have a greater impact on the analysis. Consequently, they may have caused an artificial negative trend in this region.

8. Summary and conclusions

We have reported on the quality of JRA-55 from various viewpoints. Firstly, we showed improvement in the representation of atmospheric circulation on an isentropic surface and consistency in the zonal mean field. In particular, we found that JRA-55 significantly improved the consistency of the zonal momentum budget based on the MIM method even in the stratosphere when major SSW events occur. Next, we examined the representation of atmospheric variability in several regions.

In the tropics, we found that the frequencies of high spatial correlations with TRMM3B42 are clearly higher in JRA-55 than in the NCEP/NCAR reanalysis, JRA-25, CFSR, and ERA-Interim and are close to those in MERRA. Moreover, from the results of the

wavenumber-frequency power spectrum analysis, the signals of equatorial waves and the MJO in JRA-55 are found to be much stronger than those in ERA-40 before 1978.

In the extra-tropics, we found that JRA-55 reduced the overestimation of precipitation in southeastern North America, where it was overestimated by JRA-25 in the NH warm season. Moreover, we estimated the activity of transient eddies from the 2–8-day band-pass-filtered transient eddy KE at the 300 hPa level and found that the activity of transient eddies in JRA-55 is much stronger than those in ERA-40 and the NCEP/NCAR reanalysis during the NH cold season before 1979/1980. We also examined the frequency of spatial correlation of 2–8 day band-pass-filtered daily mean OLR over the storm track regions with NOAA OLR during the NH cold season and found that JRA-55, CFSR, and ERA-Interim more frequently had high spatial correlation coefficients than MERRA, ERA-40, and JRA-25 did

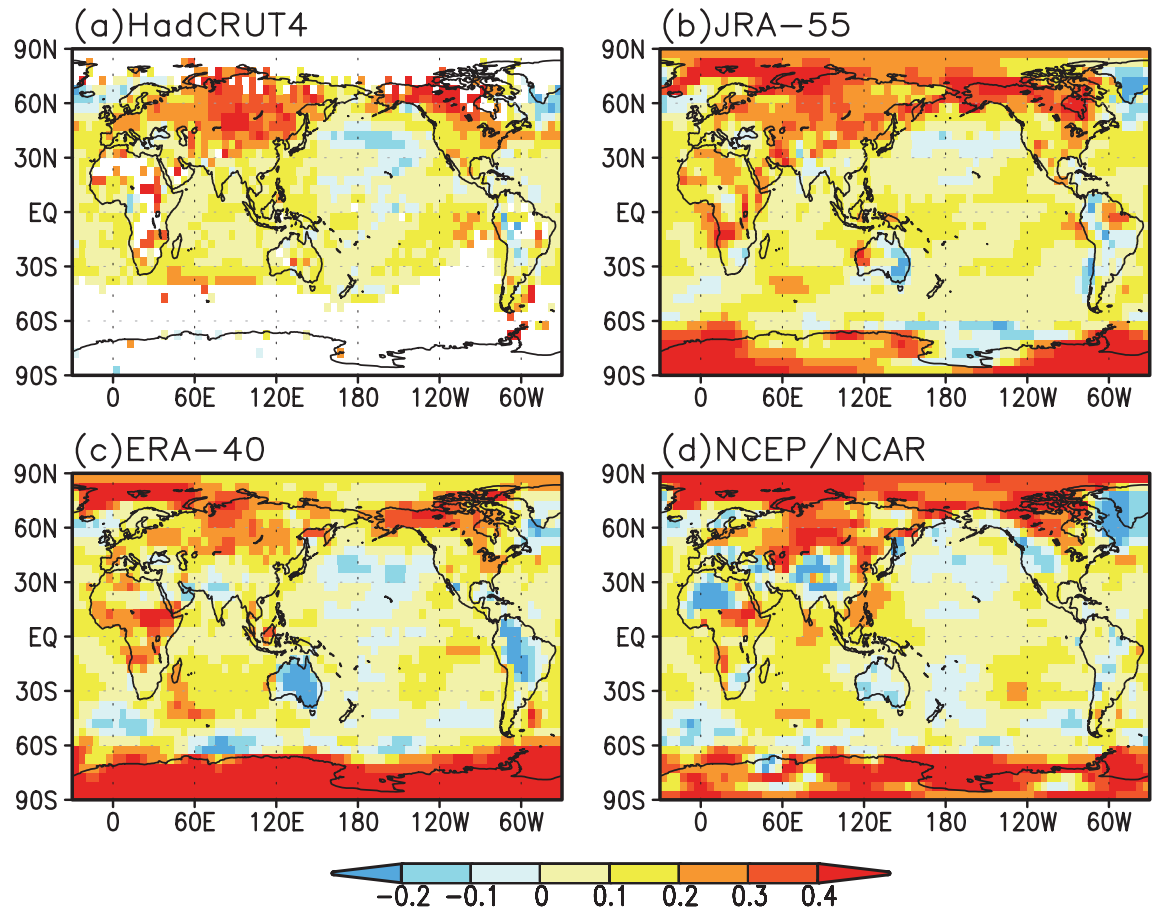


Fig. 34. Global distributions of long-term surface air temperature trends (K decade^{-1}) from 1958 to 2001. Reanalysis data were re-gridded to $5^\circ \times 5^\circ$ resolution. Trend values for HadCRUT4 were calculated only for grid boxes in which data are available for more than 80 % of investigated time period.

in the North Atlantic storm track region. This result indicates that JRA-55 significantly improved the representation of each transient eddy compared with JRA-25 in this region. In the SH cold season, JRA-55 is clearly superior to JRA-25. In addition, JRA-55 reduced the negative bias of SLP in northeastern Eurasia and improved the SLP long-term trends in the region where the Siberian High develops in boreal winter.

In the stratosphere, we found larger discrepancies between reanalyses for the extra-tropical stratosphere during the extra-tropical SH winter. Comparisons with radiosonde temperature revealed that JRA-55 has a smaller bias in temperature than the other reanalyses in the extra-tropical SH winter before 1979.

In summary, JRA-55 generally yielded improved representations over a range of space-time scales

compared with JRA-25 during the satellite era, and it improved the temporal consistency compared with ERA-40 and the NCEP/NCAR reanalysis throughout the reanalysis period. We suppose that these improvements result from major updates in the JMA operational numerical weather prediction system, such as increased resolution, the introduction of new radiation and advection schemes to the forecast model, and adaption of 4D-Var with variational bias correction to satellite radiances (Kobayashi et al. 2015).

We also found some issues in JRA-55. The amplitudes of equatorial waves and the MJO in JRA-55 are lower than those in ERA-Interim and JRA-25. In particular, the amplitude of the MJO is very low in the Indian Ocean and the western Pacific. For tropical cyclones, rapid intensification of TCs moving toward high latitudes is not properly analyzed. In the

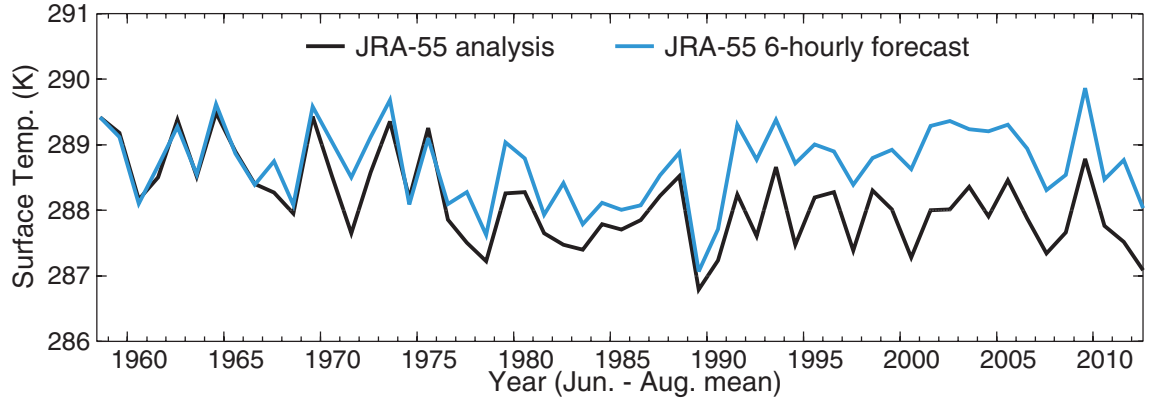


Fig. 35. Time series of surface temperature (K) averaged over 20–35°S, 140–155°E during the SH winter (June–August) from 1958 to 2012. Black and blue lines represent analysis and 6 -hourly forecast, respectively.

stratosphere, JRA-55 has a large, warm bias in the lower mesosphere, except in the polar region in the winter hemisphere. We also found that large uncertainties still exist around the stratopause and above in JRA-55, ERA-Interim, and MERRA. Moreover, in the equatorial stratosphere, the difference between reanalyses and radiosonde observations in the easterly phase at the 10 hPa and 30 hPa levels is very large, and JRA-55, ERA-40, and the NCEP/NCAR reanalysis exhibit an easterly bias when radiosonde observations indicate a weak westerly phase of the QBO before 1978. Such cases occur in the westerly acceleration phase of the QBO, and westerly accelerations in reanalyses are only about half of those in the radiosonde observations. We also found that JRA-55 and ERA-40 show unrealistic strong cooling in South America and Australia, although the spatial distribution of the long-term temperature trend in JRA-55 is the closest to HadCRUT4. To deal with these issues, it is essential to reduce the forecast model biases used in the DAS and to improve the parameterizations of physical processes. In the future, we will conduct further investigations to clarify the improvements in JRA-55 and will provide additional information on JRA-55 quality.

Acknowledgments

Verification of the JRA-55 product was supported by many JMA and MRI staff members. We would like to thank all these individuals for providing us with their invaluable help and advice. In addition, 27 independent researchers participated in quality evaluation prior to the release of the product. We sincerely appreciate their invaluable contributions.

References

- Adler, R. F., G. J. Huffman, A. Chang, R. Ferraro, P.-P. Xie, J. Janowiak, B. Rudolf, U. Schneider, S. Curtis, D. Bolvin, A. Gruber, J. Susskind, P. Arkin, and E. Nelkin, 2003: The version-2 Global Precipitation Climatology Project (GPCP) monthly precipitation analysis (1979–present). *J. Hydrometeor.*, **4**, 1147–1167.
- Allan, R., and T. Ansell, 2006: A new globally complete monthly historical gridded mean sea level pressure dataset (HadSLP2): 1850–2004. *J. Climate*, **19**, 5816–5842.
- Bell, G. D., M. S. Halpert, R. C. Schnell, R. W. Higgins, J. Lawrimore, V. E. Kousky, R. Tinker, W. Thiaw, M. Chelliah, and A. Artusa, 2000: Climate assessment for 1999. *Bull. Amer. Meteor. Soc.*, **81**, S1–S50.
- Chen, G., T. Iwasaki, H. Qin, and W. Sha, 2014: Evaluation of the warm-season diurnal variability over East Asia in recent reanalyses JRA-55, ERA-Interim, NCEP CFSR, and NASA MERRA. *J. Climate*, **27**, 5517–5537.
- Compo, G. P., J. S. Whitaker, P. D. Sardeshmukh, N. Matsui, R. J. Allan, X. Yin, B. E. Gleason, R. S. Vose, G. Rutledge, P. Bessemoulin, S. Brönnimann, M. Brunet, R. I. Crouthamel, A. N. Grant, P. Y. Groisman, P. D. Jones, M. C. Kruk, A. C. Kruger, G. J. Marshall, M. Maugeri, H. Y. Mok, Ø. Nordli, T. F. Ross, R. M. Trigo, X. L. Wang, S. D. Woodruff, and S. J. Worley, 2011: The Twentieth Century Reanalysis project. *Quart. J. Roy. Meteor. Soc.*, **137**, 1–28.
- Dee, D. P., S. M. Uppala, A. J. Simmons, P. Berrisford, P. Poli, S. Kobayashi, U. Andrae, M. A. Balmaseda, G. Balsamo, P. Bauer, P. Bechtold, A. C. M. Beljaars, L. van de Berg, J. Bidlot, N. Bormann, C. Delsol, R. Dragani, M. Fuentes, A. J. Geer, L. Haimberger, S. B.

- Healy, H., Hersbach, E. V. Hólm, L. Isaksen, P. Källberg, M. Köhler, M. Matricardi, A. P. McNally, B. M. Monge-Sanz, J.-J. Morcrette, B.-K. Park, C. Peubey, P. de Rosnay, C. Tavolato, J.-N. Thépaut, and F. Vitart, 2011: The ERA-Interim reanalysis: Configuration and performance of the data assimilation system. *Quart. J. Roy. Meteor. Soc.*, **137**, 553–597.
- Duchon, C. E., 1979: Lanczos filtering in one and two dimensions. *J. Appl. Meteor.*, **18**, 1016–1022.
- Ebdon, R. A., 1960: Notes on the wind flow at 50 mb in tropical and sub-tropical regions in January 1957 and January 1958. *Quart. J. Roy. Meteor. Soc.*, **86**, 540–542.
- Finger, F. G., and S. Teweles, 1964: The mid-winter 1963 stratospheric warming and circulation change. *J. Appl. Meteor.*, **3**, 1–15.
- Fiorino, M., 2002: Analysis and forecasts of tropical cyclones in the ECMWF 40-year reanalysis (ERA-40). *25th Conference on Hurricanes and Tropical Meteorology*, San Diego, CA, USA, 261–264.
- Fujiwara, M., J. Suzuki, A. Gettelman, M. I. Hegglin, H. Akiyoshi, and K. Shibata, 2012: Wave activity in the tropical tropopause layer in seven reanalysis and four chemistry climate model data sets. *J. Geophys. Res.*, **117**, D12105, doi:10.1029/2011JD016808.
- Gruber, A., and A. F. Kruger, 1984: The status of the NOAA outgoing longwave radiation data set. *Bull. Amer. Meteor. Soc.*, **65**, 958–962.
- Harada, Y., A. Goto, H. Hasegawa, N. Fujikawa, H. Naoe, and T. Hirooka, 2010: A major stratospheric sudden warming event in January 2009. *J. Atmos. Sci.*, **67**, 2052–2069.
- Hoskins, B. J., M. E. McIntyre, and A. W. Robertson, 1985: On the use and significance of isentropic potential vorticity maps. *Quart. J. Roy. Meteor. Soc.*, **111**, 877–946.
- Huffman, G. J., R. F. Adler, D. T. Bolvin, G. Gu, E. J. Nelkin, K. P. Bowman, Y. Hong, E. F. Stocker, and D. B. Wolff, 2007: The TRMM Multisatellite Precipitation Analysis (TMPA): Quasi-global, multiyear, combined-sensor precipitation estimates at fine scales. *J. Hydrometeor.*, **8**, 38–55.
- Iwasaki, T., 1989: A diagnostic formulation for wave-mean flow interactions and Lagrangian-mean circulation with a hybrid vertical coordinate of pressure and isentropes. *J. Meteor. Soc. Japan*, **67**, 293–312.
- Iwasaki, T., 1990: Lagrangian-mean circulation and wave-mean flow interactions of Eady's baroclinic instability waves. *J. Meteor. Soc. Japan*, **68**, 347–356.
- Iwasaki, T., 1992: General circulation diagnosis in the pressure-isentrope hybrid vertical coordinate. *J. Meteor. Soc. Japan*, **70**, 673–687.
- Iwasaki, T., 1998: A set of zonal mean equations in a pressure-isentrope hybrid vertical coordinate. *J. Atmos. Sci.*, **55**, 3000–3002.
- Iwasaki, T., H. Hamada, and K. Miyazaki, 2009: Comparisons of Brewer-Dobson circulations diagnosed from reanalyses. *J. Meteor. Soc. Japan*, **87**, 997–1006.
- Jones, P. D., D. H. Lister, T. J. Osborn, C. Harpham, M. Salmon, and C. P. Morice, 2012: Hemispheric and large-scale land surface air temperature variations: An extensive revision and an update to 2010. *J. Geophys. Res.*, **117**, D05127, doi:10.1029/2011JD017139.
- Jones, R. L., and J. A. Pyle, 1984: Observations of CH₄ and N₂O by the NIMBUS 7 SAMS: A comparison with in situ data and two-dimensional numerical model calculations. *J. Geophys. Res.*, **89**, 5263–5279.
- Kalnay, E., M. Kanamitsu, R. Kistler, W. Collins, D. Deaven, L. Gandin, M. Iredell, S. Saha, G. White, J. Woollen, Y. Zhu, M. Chelliah, W. Ebisuzaki, W. Higgins, J. Janowiak, K. C. Mo, C. Ropelewski, J. Wang, A. Leetmaa, R. Reynolds, R. Jenne, and D. Joseph, 1996: The NCEP/NCAR 40-year reanalysis project. *Bull. Amer. Meteor. Soc.*, **77**, 437–471.
- Kanamitsu, M., W. Ebisuzaki, J. Woollen, S. K. Yang, J. J. Hnilo, M. Fiorino, and G. L. Potter, 2002: NCEP–DOE AMIP-II reanalysis (R-2). *Bull. Amer. Meteor. Soc.*, **83**, 1631–1643.
- Kawatani, Y., K. Sato, T. J. Dunkerton, S. Watanabe, S. Miyahara, and M. Takahashi, 2010: The roles of equatorial trapped waves and internal inertia-gravity waves in driving the quasi-biennial oscillation. Part I: Zonal mean wave forcing. *J. Atmos. Sci.*, **67**, 963–980.
- Kennedy, J. J., N. A. Rayner, R. O. Smith, D. E. Parker, and M. Saunby, 2011a: Reassessing biases and other uncertainties in sea-surface temperature observations measured in situ since 1850: 1. Measurement and sampling errors. *J. Geophys. Res.*, **116**, D14103, doi:10.1029/2010JD015218.
- Kennedy, J. J., N. A. Rayner, R. O. Smith, D. E. Parker, and M. Saunby, 2011b: Reassessing biases and other uncertainties in sea-surface temperature observations measured in situ since 1850: 2. Biases and homogenization. *J. Geophys. Res.*, **116**, D14104, doi:10.1029/2010JD015220.
- Kim, D., M. I. Lee, D. Kim, S. D. Schubert, D. E. Waliser, and B. Tian, 2014: Representation of tropical subseasonal variability of precipitation in global reanalyses. *Climate Dyn.*, **43**, 517–534.
- Kistler, R., E. Kalnay, W. Collins, S. Saha, G. White, J. Woollen, M. Chelliah, W. Ebisuzaki, M. Kanamitsu, V. Kousky, H. van den Dool, R. Jenne, and M. Fiorino, 2001: The NCEP-NCAR 50-year reanalysis: Monthly means CD-ROM and documentation. *Bull. Amer. Meteor. Soc.*, **82**, 247–267.
- Kobayashi, C., and T. Iwasaki, 2016: Brewer-Dobson circulation diagnosed from JRA-55. *J. Geophys. Res.*, **121**, doi:10.1002/2015JD023476.
- Kobayashi, C., H. Endo, Y. Ota, S. Kobayashi, H. Onoda, Y. Harada, K. Onogi, and H. Kamahori, 2014: Preliminary results of the JRA-55C, an atmospheric reanal-

- ysis assimilating conventional observations only. *SOLA*, **10**, 78–82.
- Kobayashi, S., Y. Ota, Y. Harada, A. Ebita, M. Moriya, H. Onoda, K. Onogi, H. Kamahori, C. Kobayashi, H. Endo, K. Miyaoka, and K. Takahashi, 2015: The JRA-55 Reanalysis: General specifications and basic characteristics. *J. Meteor. Soc. Japan*, **93**, 5–48.
- Liebmann, B., and C. A. Smith, 1996: Description of a complete (interpolated) outgoing longwave radiation dataset. *Bull. Amer. Meteor. Soc.*, **77**, 1275–1277.
- Mitchell, D. M., L. J. Gray, M. Fujiwara, T. Hibino, J. A. Anstey, W. Ebisuzaki, Y. Harada, C. Long, S. Misios, P. A. Stott, and D. Tan, 2015: Signatures of naturally induced variability in the atmosphere using multiple reanalyses datasets. *Quart. J. Roy. Meteor. Soc.*, **141**, 2011–2031.
- Morice, C. P., J. J. Kennedy, N. A. Rayner, and P. D. Jones, 2012: Quantifying uncertainties in global and regional temperature change using an ensemble of observational estimates: The HadCRUT4 data set. *J. Geophys. Res.*, **117**, D08101, doi:10.1029/2011JD017187.
- Murakami, T., 2014: Tropical cyclones in reanalysis data sets. *Geophys. Res. Lett.*, **41**, 2133–2141.
- Nakamura, H., T. Sampe, A. Goto, W. Ohfuchi, and S.-P. Xie, 2008: On the importance of midlatitude oceanic frontal zones for the mean state and dominant variability in the tropospheric circulation. *Geophys. Res. Lett.*, **35**, L15709, doi:10.1029/2008GL034010.
- Nicholson, S. E., B. Some, J. McCollum, E. Nelkin, D. Klotter, Y. Berte, B. M. Diallo, I. Gaye, G. Kpabeba, O. Ndiaye, J. N. Noukpozounkou, M. M. Tanu, A. Thiam, A. A. Toure, and A. K. Traore, 2003a: Validation of TRMM and other rainfall estimates with a high-density gauge dataset for West Africa. Part I: Validation of GPCC rainfall product and pre-TRMM satellite and blended products. *J. Appl. Meteor.*, **42**, 1337–1354.
- Nicholson, S. E., B. Some, J. McCollum, E. Nelkin, D. Klotter, Y. Berte, B. M. Diallo, I. Gaye, G. Kpabeba, O. Ndiaye, J. N. Noukpozounkou, M. M. Tanu, A. Thiam, A. A. Toure, and A. K. Traore, 2003b: Validation of TRMM and other rainfall estimates with a high-density gauge dataset for West Africa. Part II: Validation of TRMM rainfall products. *J. Appl. Meteor.*, **42**, 1355–1368.
- Onogi, K., J. Tsutsui, H. Koide, M. Sakamoto, S. Kobayashi, H. Matsushika, T. Matsumoto, N. Yamazaki, H. Kamahori, K. Takahashi, S. Kadokura, K. Wada, K. Kato, R. Oyama, T. Ose, N. Mannaji, and R. Taira, 2007: The JRA-25 Reanalysis. *J. Meteor. Soc. Japan*, **85**, 369–432.
- Reed, R. J., 1965: The quasi-biennial oscillation of the atmosphere between 30 and 50 km over Ascension Island. *J. Atmos. Sci.*, **22**, 331–333.
- Rienecker, M. M., M. J. Suarez, R. Gelaro, R. Todling, J. Bacmeister, E. Liu, M. G. Bosilovich, S. D. Schubert, L. Takacs, G.-K. Kim, S. Bloom, J. Chen, D. Collins, A. Conaty, A. da Silva, W. Gu, J. Joiner, R. D. Koster, R. Lucchesi, A. Molod, T. Owens, S. Pawson, P. Pegion, C. R. Redder, R. Reichle, F. R. Robertson, A. G. Ruddick, M. Sienkiewicz, and J. Woollen, 2011: MERRA: NASA's Modern-Era Retrospective Analysis for Research and Applications. *J. Climate*, **24**, 3624–3648.
- Ritchie, H., 1985: Application of a semi-Lagrangian integration scheme to the moisture equation in a regional forecast model. *Mon. Wea. Rev.*, **113**, 424–435.
- Saha, S., S. Moorthi, H.-L. Pan, X. Wu, J. Wang, S. Nadiga, P. Tripp, R. Kistler, J. Woollen, D. Behringer, H. Liu, D. Stokes, R. Grumbine, G. Gayno, Y.-T. Hou, H.-Y. Chuang, H.-M. H. Juang, J. Sela, M. Iredell, R. Treadon, D. Kleist, P. van Delst, D. Keyser, J. Derber, M. Ek, J. Meng, H. Wei, R. Yang, S. Lord, H. van den Dool, A. Kumar, W. Wang, C. Long, M. Chelliah, Y. Xue, B. Huang, J.-K. Schemm, W. Ebisuzaki, R. Lin, P. Xie, M. Chen, S. Zhou, W. Higgins, C.-Z. Zou, Q. Liu, Y. Chen, Y. Han, L. Cucurull, R. W. Reynolds, G. Rutledge, and M. Goldberg, 2010: The NCEP climate forecast system reanalysis. *Bull. Amer. Meteor. Soc.*, **91**, 1015–1057.
- Sampe, T., H. Nakamura, A. Goto, and W. Ohfuchi, 2010: Significance of a midlatitude SST frontal zone in the formation of a storm track and an eddy-driven westerly jet. *J. Climate*, **23**, 1793–1814.
- Schenkel, B. A., and R. E. Hart, 2012: An examination of tropical cyclone position, intensity, and intensity life cycle within atmospheric reanalysis datasets. *J. Climate*, **25**, 3453–3475.
- Schneider, U., A. Becker, P. Finger, A. Meyer-Christoffer, B. Rudolf, and M. Ziese, 2011: *GPCC full data reanalysis version 6.0 at 0.5°: Monthly land-surface precipitation from rain-gauges built on GTS-based and historic data*. doi:10.5676/DWD_GPCC/FD_M_V6_050.
- Tanaka, D., T. Iwasaki, S. Uno, M. Ujiie, and K. Miyazaki, 2004: Eliassen–Palm flux diagnosis based on isentropic representation. *J. Atmos. Sci.*, **61**, 2370–2383.
- Ten, H., G. Branstator, H. Wang, G. A. Meehl, and W. M. Washington, 2013: Probability of US heat waves affected by a subseasonal planetary wave pattern. *Nat. Geosci.*, **6**, 1056–1061.
- Uppala, S. M., P. W. Källberg, A. J. Simmons, U. Andrae, V. da Costa Bechtold, M. Fiorino, J. K. Gibson, J. Haseler, A. Hernandez, G. A. Kelly, X. Li, K. Onogi, S. Saarinen, N. Sokka, R. P. Allan, E. Andersson, K. Arpe, M. A. Balmaseda, A. C. M. Beljaars, L. van de Berg, J. Bidlot, N. Bormann, S. Caires, F. Chevallier, A. Dethof, M. Dragosavac, M. Fisher, M. Fuentes, S. Hagemann, E. Hólm, B. J. Hoskins, L. Isaksen, P. A. E. M. Janssen, R. Jenne, A. P. McNally, J.-F. Mahfouf, J.-J. Morcrette, N. A. Rayner, R. W. Saun-

- ders, P. Simon, A. Sterl, K. E. Trenberth, A. Untch, D. Vasiljevic, P. Viterbo, and J. Woollen, 2005: The ERA-40 re-analysis. *Quart. J. Roy. Meteor. Soc.*, **131**, 2961–3012.
- Waters, J. W., L. Froidevaux, R. S. Harwood, R. F. Jarnot, H. M. Pickett, W. G. Read, P. H. Siegel, R. E. Cofield, M. J. Filipiak, D. A. Flower, J. R. Holden, G. K. Lau, N. J. Livesey, G. L. Manney, H. C. Pumphrey, M. L. Santee, D. L. Wu, D. T. Cuddy, R. R. Lay, M. S. Loo, V. S. Perun, M. J. Schwartz, P. C. Stek, R. P. Thurstans, M. A. Boyles, K. M. Chandra, M. C. Chavez, G.-S. Chen, B. V. Chudasama, R. Dodge, R. A. Fuller, M. A. Girard, J. H. Jiang, Y. Jiang, B. W. Knosp, R. C. LaBelle, J. C. Lam, K. A. Lee, D. Miller, J. E. Oswald, N. C. Patel, D. M. Pukala, O. Quintero, D. M. Scaff, W. van Snyder, M. C. Tope, P. A. Wagner, and M. J. Walch, 2006: The Earth Observing System Microwave Limb Sounder (EOS MLS) on the Aura satellite. *IEEE Trans. Geosci. Remote Sens.*, **44**, 1075–1092.
- Wheeler, M., and G. N. Kiladis, 1999: Convectively coupled equatorial waves: Analysis of clouds and temperature in the wavenumber–frequency domain. *J. Atmos. Sci.*, **56**, 374–399.
- Worley, S. J., S. D. Woodruff, R. W. Reynolds, S. J. Lubker, and N. Lott, 2005: ICOADS Release 2.1 data and products. *Int. J. Climatol.*, **25**, 823–842.
- Yokoi, S., 2015: Multi-reanalysis comparison of variability in column water vapor and its analysis increment associated with Madden–Julian oscillation. *J. Climate*, **28**, 793–808.